Optical and electrical modeling of polymer:fullerene bulk heterojunction solar cells

Jan Derk Kotlarski

Optical and electrical modeling of polymer:fullerene bulk heterojunction solar cells
Jan Derk Kotlarski

PhD Thesis
University of Groningen

Zernike Institute PhD Thesis Series 2012-11

ISSN: 1570-1530

ISBN: 978-90-367-5481-1 (print)

ISBN: 978-90-367-5480-4 (digital)

university of groningen / faculty of mathematics and natural sciences / zernike institute for advanced materials

The research described in this thesis was performed in the research group Molecular Electronics: Physics of Organic Semiconductors of the Zernike Institute for Advanced Materials at the University of Groningen, the Netherlands. The project was financially supported by the Zernike Institute for Advanced Materials.

RIJKSUNIVERSITEIT GRONINGEN

Optical and electrical modeling of polymer:fullerene bulk heterojunction solar cells

Proefschrift

ter verkrijging van het doctoraat in de
Wiskunde en Natuurwetenschappen
aan de Rijksuniversiteit Groningen
op gezag van de
Rector Magnificus, dr. E. Sterken,
in het openbaar te verdedigen op
vrijdag 27 april 2012
om 16:15 uur

door

Jan Derk Kotlarski

geboren op 15 mei 1977
te Emmen

Promotor:	Prof.dr.ir. P.W.M. Blom
Beoordelingscommissie:	Prof.dr. R.A.J. Janssen Prof.dr.ir. P.H.M. van Loosdrecht Prof.dr.ir. M. Zeman

CONTENTS

Contents

Chapter 1

Basics of organic solar cell operation

Summary

The worldwide demand for usable energy increases year after year and feasible alternatives for fossil fuels need to be employed in order meet that demand. Organic photovoltaics are expected to contribute in meeting that demand and are already in commercial production. This introductory chapter describes why polymer based solar cells are interesting for commercial use, what their basic operation principle is and how they are characterized. Furthermore, a more advanced theory underlying their working principle is given. Finally an outline of the thesis is given.

1.1 Solar power

The world's demand for usable energy increases every year, with an expected increase from 479 trillion joule (505 quadrillion Btu) in 2008 to 730 trillion joule (770 quadrillion Btu) in 2035[1], an increase of 52 %. In order to meet this demand, nonrenewable fossil fuels, mostly coal, and renewable sources of useful energy will need to be deployed. As fossil fuels will eventually run out and their use is seen as the main contributor to the increase of the global greenhouse effect, more research is done on the development and deployment of alternative technologies for renewable energy production.

Sunlight is an abundant and virtually eternally renewable energy source, with 174 petawatt of power arriving at the earth's atmosphere and about 89 petawatt being absorbed by land and water. Even using only a fraction of this enormous amount of power may significantly meet the world's growing demand for power. Solar cells, which rely on the photovoltaic effect, transform sunlight into electricity and in order to successfully utilize solar power, developing well performing and cost-effective photovoltaic devices is paramount.

Solar cells can be categorized into two different kinds, inorganic and organic ones. The former having a current commercial power efficiency between 15 and 20 %[2], up to 25 % for more refined silicon cells[2] and top lab-scale efficiencies of more than 40 % being reached with lab-scale multijunction devices consisting of various inorganic semiconductors and the usage of light concentration techniques.[2] However, the performance of organic solar cells is considerably lower with a commercial efficiency of about 3 to 5 %[3] and a current top efficiency of 8.3 %[2]. Producing inorganic solar cells requires a substantial initial investment of materials, energy and finances, of which the energy and finances are recouped and exceeded only after several years of operation. Still inorganic solar cells produce energy in their lifetime at a significantly greater cost than conventional and other nonconventional energy sources, so research is performed to decrease the costs and increase the energetic yields. One contribution to the high costs of inorganic solar cells is that the materials and their purification are costly, even for the commercially available photovoltaic

devices. Organic solar cells look promising in the sense that their production costs in materials, energy and finances are assumed to be much lower when in commercial production, but some hurdles are already experienced, their low efficiency, a maximum of 8.3 %[2] in laboratory settings, and their relatively low lifetime due to device instability. Yet as the field of organic solar cells is still under development and recent improvements drive their performance towards new records approaching efficiencies of 10%, the expectation is that organic photovoltaics may bring cheap, mass-producible and relatively efficient renewable energy sources to the market.

1.2 Organic semiconductors

In 1977 Shirakawa, MacDiarmid, and Heeger discovered (semi)conductance in highly doped conjugated polymers and demonstrated that their conductance could be controlled by adjusting the doping.[4] This has been the birth ground for a new field of electronics based on organic materials, where conjugated materials, which have alternating single and double carbon bonds, are either small molecules or polymers. The three main bonds of carbon atoms in the backbone of the conjugated material are σ-bonds, with tightly bound and thus localized electrons. The p_z orbitals that form the fourth valance of the carbon atoms interact with each other and form π-bonds, conjugated with each other along the backbone in such a way that a collective π-system is formed, consisting of delocalized electrons. These delocalized electrons are associated with a molecular orbital and as energy minimization due to bond length alternation makes the material an intrinsic semiconductor, the unexcited π-band is completely filled and has a top edge coinciding with the highest occupied molecular orbital (HOMO). The bottom edge of the empty excited π*-band is thus the lowest unoccupied molecular orbital and is situated above the energy gap. Supplying sufficient energy to an electron promotes it from the HOMO to the LUMO level, in such creating an exciton, essentially a bound electron-hole pair in the conjugated material. The band gap between LUMO and HOMO levels for organic semiconductors is typically between 1 and 4 eV and dependent on their chemical structure. Figure 1.1 shows a few notable organic conjugated molecules in structure form.

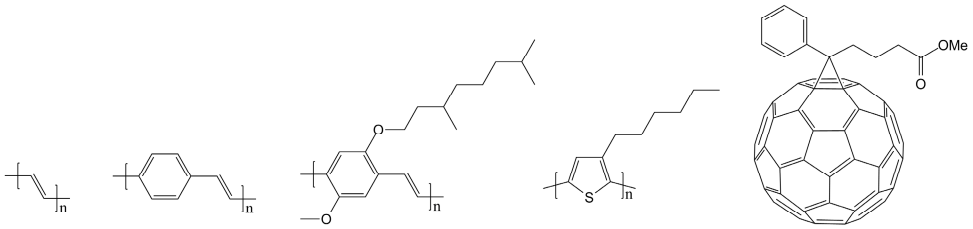

(a) PA (b) PPV (c) MDMO-PPV (d) P3HT (e) PCBM

Figure 1.1: Molecular structures and abbreviations for four conjugated polymers and a small molecule. (a) poly(acetylene) PA, (b) poly(*p*-phenylene-vinylene) PPV, (c) a PPV with substitution (MDMO-PPV), (d) poly(3-hexyl thiophene) P3HT and (e) a derivative of C_{60} (PCBM). Note that the alternating single and double bonds in the compounds give rise to their semiconductance.

1.3 Organic solar cells

As conjugated polymers have a relatively high extinction coefficient when compared to typical inorganic semiconductors, most conjugated polymers are able to absorb a large fraction of the incident solar light, of which the energy coincides with their absorption band, in layers thinner than a hundred nanometers, which makes material cost reduction feasible.[5] Another great advantage of conjugated polymers comes from their compatibility with affordable printing and coating techniques that is due to the favorable solubility properties of most conjugated polymers. In this it might seem that the processes of printing and coating conjugated polymers from solution might affect the film formation properties negatively. It has been found that a certain degree of spontaneous self-organization of the materials inside the active layer is necessary in order for an solution-processed solar cell to perform well.[6] This property of modern polymer solar cells has become an intrinsic part of their design, being the result of a series of important advances in organic photovoltaics.

The field of organic photovoltaics dates back to 1959, when Kallmann and Pope discovered the photovoltaic properties of anthracene, which in a solar cell however performed very poorly.[7] After many years, the efficiency of organic solar cells having a single layer of organic molecules was still quite low (< 1 %)[8,9] and the

performance of polymer-based diodes was even lower.[10,11] This low performance originated from the fact that absorbed photons do not generate excitations that directly separate into free charges, but instead generate tightly bound excitons, as previously discussed, with a binding energy of about 0.4 eV. Due to the low dielectric constant in organic semiconductors, this large binding energy effectively prevents the dissociation of these excitons for typical electric field strengths encountered in these devices. In such, the overbearing majority of excitons in a single layer of a conjugated polymer decay instead of dissociating into free charges at room temperature.[5]

In order to make exciton dissociation and subsequent charge separation not only more probable and permanent as well, a so called donor – acceptor (D – A) system can be implemented, as Tang demonstrated in 1986.[12] Donor – acceptor systems consist of at least one material that is a photoactive organic semiconductor and another material that is a different organic semiconductor with LUMO and HOMO levels energetically arranged in such a way, that electron transfer from the donor to the acceptor material is favored and/or hole transfer from the acceptor to the donor is favored. Excitons encountering the donor – acceptor boundary undergo ultrafast charge transfer from the layer they reside in to the other layer, in such dissociating into spatially separated yet still electrically bound electron – hole pairs, a process with near unity probability. The reverse process is very improbable, as it is energetically unfavorable. In a donor – acceptor system both donor and acceptor are photo-active, where the donor – acceptor systems studied in this thesis consist of photoactive polymers as electron donors and less photo-active fullerenes as electron acceptors. These systems were chosen as they have come into increasing scientific focus since Sariciftci et al. reported picosecond photoinduced charge transfer from a conjugated polymer onto buckminsterfullerene (C_{60}).[13] The bilayer donor – acceptor device structure was successful, yet has a big drawback in the form of a limited amount of generated excitons diffusing to the donor – acceptor boundary, as the excitons have a short decay time and thus a short effective diffusion length. In conjugated polymers this diffusion length is in the order of 5 – 10 nm,[14,15] making the performance of bilayer devices fully dependent on the excitons generated near the donor – acceptor interface.

A way to majorly increase the number of excitons reaching the donor – acceptor interface is the bulk heterojunction (BHJ) design.[16] The concept behind it is

the foundation for modern most efficient polymer solar cells and consists of the blending of both donor and acceptor materials in order to produce a composite layer with nanoscale donor and acceptor domains that have a large interfacial area. Excitons generated in the active domains have a highly increased probability diffusing to a donor – acceptor interface before they decay. Transport of separated charges to the electrodes necessitates an interpenetrating network of donor and acceptor, which relies on a minimum amount of percolation, thus the performance of a BHJ cell is very dependent of the morphology of the donor – acceptor system. In 2001 Shaheen et al. highlighted the importance of morphology by demonstrating the near threefold increase in efficiency of polymer solar cells by only changing the shared solvent used to spin-coat the active layer from the conjugated polymer and a soluble C_{60} derivative.[17] Since then it has been found that the right processing methods and processes allow for many donor – acceptor material combinations to have a tendency to phase separate into a network of domains with suitable domain sizes when used in solution processed polymer solar cells.[6] This advantageous property of the BHJ polymer solar cell makes it a favorable candidate for the development of well performing solution-processed organic photovoltaics.

1.4 Device structure and performance characterization

In this thesis we will focus on polymer:fullerene BHJ solar cells, which are commonly used due to their tunability in many of their properties, like optical and electrical band gaps, electrical conductivity and good solvability in various solvents. The mostly used device structure consists of a glass substrate of 0.7 to 1 mm thickness with on top of it a patterned and sputtered layer of indium tin oxide (ITO) of about 130 to 140 nm thickness serving as a transparent highly conductive electrical contact with a stack of several layers deposited on top of it. For single cell devices this stack consists of a transparent material layer functioning as a transparent electrode extracting either electrons or holes, then the semi-transparent BHJ polymer:fullerene

material used for the absorption of photons and their conversion to free charge carriers, finished by a layer of highly reflective and electrically conductive material functioning as an electrode extracting either holes or electrons, as an electric contact and reflecting light back towards the active layer. Figure 1.2 shows a typical single device structure.

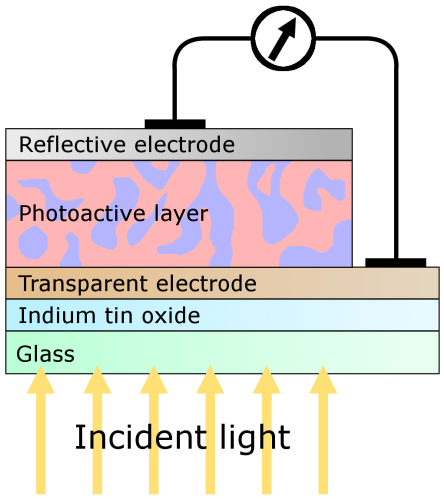

Figure 1.2: Schematic layout of a typical device structure for a bulk heterojunction solar cell. The light enters the structure through the glass substrate.

A typical stack structure used for efficient cells in the past years has been glass/ITO with poly(3,4-ethylenedioxythiophene) poly(styrenesulfonate) (PEDOT:PSS) spin-coated on it as a transparent anode with a thickness of typically 40 nm, then a bulk heterojunction of poly(3-hexylthiophene):6,6-phenyl C_{61}-butyric acid methyl ester (P3HT:PCBM) with thicknesses varying between 50 to 300 nm and finally an evaporated lithiumfluoride(LiF)\aluminum(Al) reflective cathode, with LiF being about 1 nm thick and Al about 100 nm thick. Tandem solar cell device structures typically have a similar base consisting of glass/ITO substrate and a stack containing two active layers on top of that. This stack is similar to the stack of the single cell device but has additionally on top of the first active layer a transparent middle electrode, followed by a second active layer of a bulk heterojunction material with an absorption spectrum complementary to that of the first active layer, covered by a reflective electrode, that either extracts holes or electrons, depending on the device geometry.

Characterization of solar cell performance is done by measuring the dependence of current density on applied voltage ($J - V$) under certain fixed standard conditions. In this thesis we assume these conditions to be the temperature of the device of 298 K, an average solar light intensity being 1000 W/m^2 and the spectral distribution of solar light being the solar light spectrum after it has passed through 1.5 times the thickness of the atmosphere, which is called air mass 1.5 or AM1.5 solar spectrum. Figure 1.3 shows typical $J - V$ characteristics of an organic solar cell, from which the four characterization parameters can be deduced.

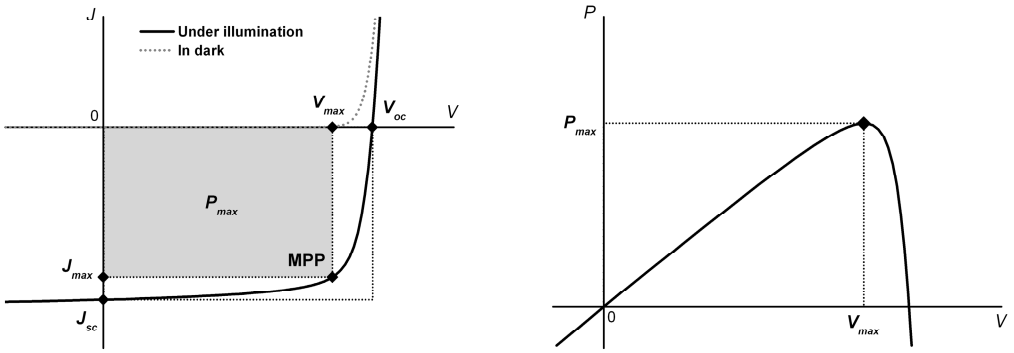

Figure 1.3: *Left:* Typical $J - V$ curve of an illuminated polymer solar cell. The parameters pertaining to the cell's performance are shown in the figure and explained in the text. *Right:* Output power of the solar cell plotted as a function of voltage, P_{max} and thus MPP are determined from this curve.

Two are either measured or interpolated, which are the current density measured at zero applied bias voltage called the short-circuit density J_{sc} and the applied voltage at which the current density is zero called the open-circuit voltage V_{oc}. The fill factor FF is defined as the maximum power P_{max} that the device can deliver divided by the multiplication product of short-circuit current density and open-circuit voltage:

$$FF = \frac{P_{Max}}{V_{oc} J_{sc}} = \frac{V_{\max} J_{\max}}{V_{oc} J_{sc}} \tag{1.1}$$

The power conversion efficiency PCE is the maximum power deliverable by the device divided by the incident light power P_{in}:

$$PCE = \frac{P_{\max}}{P_{in}} = \frac{V_{oc} J_{sc} FF}{P_{in}} \tag{1.2}$$

1.5 Charge transport and electric modeling

Investigations into the charge transport properties of many conjugated semiconductors have shown that the drift mobility μ is activated and has a stretched-exponential dependence on the electric field:[18-22]

$$\mu(E) = \mu(0) \exp\left(\gamma \sqrt{E}\right) \tag{1.3}$$

where $\mu(0)$ is the zero field mobility and γ is a field activation parameter. This relation is assumed to stem from the hopping of charges between localized states having a Gaussian distribution of energy levels, as presented by Bässler.[23] In order to come to a better agreement between the model and experimental data at low electrical field conditions, long-range spatial correlations of the site energies were included in the model[24] and this correlated Gaussian disorder model explains the $\ln \mu \propto \sqrt{E}$ dependence and predicts a non-Arrhenius temperature dependence of $\ln \mu \propto T^{-2}$.[25,26] Using ohmic contacts to readily inject and extract sufficiently large numbers of charge carriers in an conjugated polymer, the resulting current flow will be space charge limited (SCL).[27] The relation between the applied voltage and resulting space charge limited current density J_{SCL} is mediated by the thickness of the semiconducting layer and the charge carrier mobility and is given by the Mott-Gurney law:[28]

$$J_{SCL} = \frac{9}{8} \varepsilon_0 \varepsilon_r \mu \frac{V^2}{L^3} \tag{1.4}$$

where V is the potential difference across the material, L is the thickness of the material and $\varepsilon_0 \varepsilon_r$ is the dielectric parameter of the material. Shortly after the validity of

the Mott-Gurney law for organic semiconductors was confirmed, deviations from this law were measured in single charge carrier devices made of a poly(*p*-phenylene vinylene) (PPV) derivative and attributed to a field-activated mobility increase as given by Eq. (1.3).[29,30] Later it was shown that at room temperature the increase of mobility with voltage is governed by an increase in charge carrier density in the device, while the increase of mobility through the electric field dependence is more pronounced at lower temperatures.[31] Additionally, the zero-field mobility $\mu(0)$ has been found to be activated as given by the following relation:

$$\mu(0) = \mu_0 \exp\left(-\frac{\Delta}{kT}\right) \tag{1.5}$$

where μ_0 is the mobility in the zero-field limit and $T \to \infty$, Δ is the activation energy and k is Boltzmann's constant. The correlated Gaussian disorder model can explain the Arrhenius-type activation when taking into account the effect of background charges being injected into the organic semiconductor from the ohmic contacts.[32,33] μ_0 has been experimentally found to be a universal constant ($\mu_0 = 3 \times 10^3$ m^2/Vs) for a diverse number of conjugated polymers, allowing for the determination of Δ from the value of $\mu(0)$ for only one temperature T_1 using:

$$\Delta = kT \ln\left(\frac{\mu_0}{\mu(0)}\right)\Bigg|_{T=T_1} \tag{1.6}$$

The charge carrier density in the active layer of polymer solar cells under normal operating conditions is typically less than 10^{22} m^{-3}. As the mobility is nearly constant for these densities, its density dependence plays only a minor role and may be ignored to understand the basic operation.

1.6 Device physics and operation

The further development of polymer solar cells hinges upon a thorough understanding of the fundamental processes that define the workings of these devices and in such impact their performance. These devices exhibit a strong dependence of the photocurrent density on the applied voltage, which is clearly shown by the fill factor of typically 65 % in which the field-dependent charge generation mechanism in these devices plays a role. Figure 1.4 shows a schematic summary of the processes governing photocurrent generation in a bulk heterojunction solar cell.[34,35].

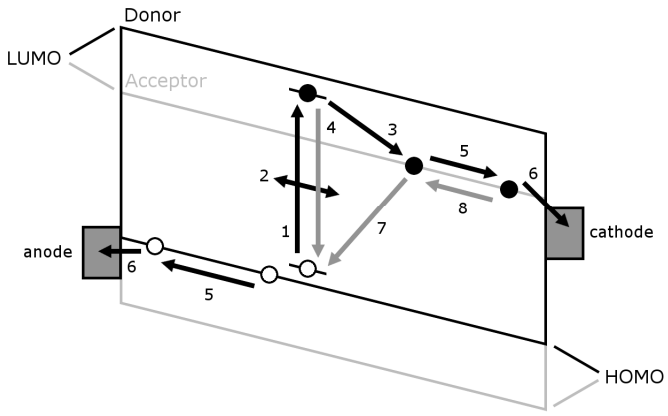

Figure 1.4: Schematic operation of a bulk heterojunction solar cell for near short-circuit conditions. The processes occurring are (1) exciton generation, (2) exciton diffusion, (3) ultrafast charge transfer, (4) exciton decay, (5) free charge transport, (6) charge extraction by the electrodes, (7) geminate recombination of bound charge pairs, and bimolecular recombination of free charges resulting in a bound charge pair.

Photoexcitation of the polymer [**1**] leads to the generation of an exciton that diffuses through the polymer [**2**] until it encounters the donor – acceptor interface where it dissociates due to ultrafast charge transfer [**3**], or it decays to the ground state before it reaches an interface [**4**], which might be situated too far away. When the latter occurs, the excitation energy is lost and there is no contribution to the photocurrent. When the former occurs, a bound electron – hole pair is formed, which with the possible help of an external electric field and thermal activation can dissociate into free carriers of opposite charge, residing in the two distinct material phases (i.e., a hole in the donor and an electron in the acceptor). The material phases conduct the free charges to the

electrodes [**5**], where they are extracted [**6**] and can be put to use in an external circuit. Still, bound electron – hole pairs at the donor-acceptor interface have a finite lifetime because they can decay to the ground state through geminate recombination [**7**], wherein the charge carriers are lost. Free carriers can become a bound pair through bimolecular recombination [**8**], which then can either dissociate again or decay to the ground state.

1.7 Electrical modeling

The simulation work done in this thesis leans on two models, one optical and one electrical, which are combined together to fully simulate polymer:fullerene BHJ solar cell devices from specific parametric input. The optical model, based upon the transfer matrix approach as proposed by Knittl[36] and implemented by Petterson et al.,[37] will be discussed in chapter two of this thesis. The electrical model is based on a numerical device model as developed by Koster et al.[38], that will be shortly discussed here. This electrical model can be used to describe the current-voltage characteristics of polymer:fullerene bulk heterojunction solar cells as well as those of hybrid[39] and all-polymer solar cells.[40] In the model the BHJ solar cell is described as a metal-insulator-metal system, which is based on an effective medium approach treating the active blend layer as one intrinsic semiconductor. By numerically solving the basic semiconductor continuity and Poisson equations the current-voltage relations can be calculated. The semiconductor equations describe drift, diffusion, dependence of the internal electric field on space charge, bimolecular recombination of free charges and a dissociation rate of bound electron-hole pairs dependent on temperature and the internal electric field.

When modeling the device characteristics, the experimental data can be conveniently represented by plotting the photocurrent density J_{ph}, which is the current density under illumination J_L minus the current density in the dark J_D, as a function of the effective voltage over the cell $V_0 - V_A$. Here, V_A is the applied voltage and V_0 the compensation voltage, where $J_{ph}(V_A = V_0) = 0$. V_0 is usually tens of millivolts higher

than V_{oc}. Three different regimes can be observed when the $J - V$ data is plotted with double-logarithmic axes, as shown in figure 1.5.

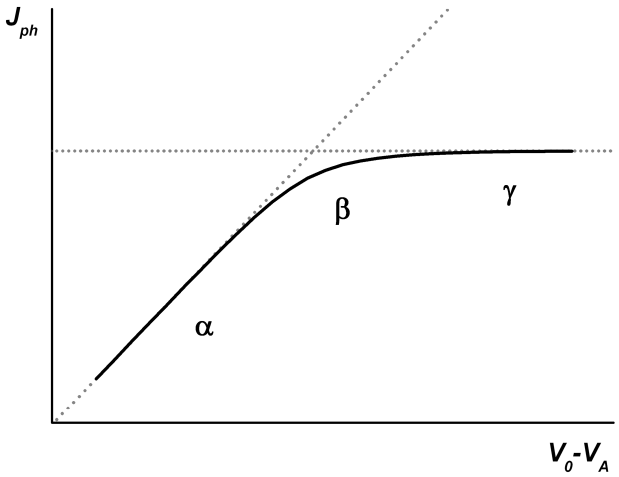

Figure 1.5: Typical shape for a J_{ph} versus V_0 - V_A curve. The three denoted regimes are described in the text.

The first regime is for low effective voltages (region **α**), where drift and diffusion currents are at equilibrium and result in a linear dependence of J_{ph} on $V_0 - V_A$. For high voltages, the third regime (region **γ**), drift currents dominate the photocurrent and observations show that J_{ph} saturates, as all photogenerated charges are extracted through the electrodes. Between these clear regimes is the second regime (region **β**), where J_{ph} gradually increases and is determined by drift, diffusion, recombination as well as the field-dependent dissociation probability of bound photogenerated bound electron-hole pairs.[34] The charge transport parameters for the holes in the donor and electron in the acceptor are experimentally determined from test devices using selective electrical contacts, resulting in so-called hole-only or electron-only devices. By fitting experimentally obtained data with this numerical device model for various temperatures and light intensities, more understanding is obtained regarding the operation of the solar cell under various circumstances. Combined with the optical model the obtained electrical parameters then allow us to simulate cells in order to predict their performance for other stack designs or under other operating conditions, as will be demonstrated in the remainder of this thesis

1.8 Tandem polymer:fullerene solar cells

Single layer polymer cells have several fundamental limitations to their performance when considering them from an optical standpoint. A typically wide band gap energy of E_{gap} ~ 2 eV is found among many well-studied conjugated polymers and as only photons with en energy equal to or higher than that of the band gap can be absorbed, that limits the absorption spectrum and in such the maximum amount of photocurrent extractable from the device. By using polymers with a smaller band gap the performance of the solar cells is expected to increase since lower wavelength photons are also converted into charge carriers and in such increasing the short-circuit current density.[41-45] A major tradeoff for using these polymers with smaller band gaps is in the form of a declining open-circuit voltage for increasing current density of a single layer solar cell. Absorbed photons with high energy $hv > E_{gap}$ give rise to hot excitons that lose excess energy via thermalization and the generated charge carriers will be collected at the contacts with a potential difference between electrons and holes of $V \leq E_{gap}^{eff}/q$, where E_{gap}^{eff} is the effective band gap, the energy difference between the HOMO level of the donor and the LUMO level of the acceptor. For the case that the effective bad gap is reduced by lowering the band gap of the absorber the gain of a small band gap device being able to generate higher current densities than a wide band gap device is diminished by the loss of maximum open-circuit voltage.

A way to circumvent this drawback is to stack two or more bulk heterojunction layers with complementary absorption spectra on top of each other in a single device, in such decreasing these losses and absorbing photons over a wider absorption range. Photon energy loss through thermalization is diminished through the use of multiple active layers with different band gaps and the limitations to layer thicknesses due to low charge carrier mobilities can be accommodated with the use of thin multiple layers.

Using multiple junctions in the field of OPV is not entirely new,[46,47] yet it was first in 2006 that the use of two polymer based bulk heterojunction layers with distinct and complementary absorption spectra in a device was reported. In that year,

Hadipour et al.[48] proposed a tandem cell structure wherein a composite metallic middle electrode was used as an electron and hole ohmic contact for the front and back cell respectively. Furthermore the metallic layers provided protection for the front active layer while the back active layer was spin coated on top of them, as both active layers were spin coated from the same solvent. The sub-cells were connected in series, resulting in a low short-circuit current density that was limited to the lower short-circuit current density of the back sub-cell and an open-circuit voltage that is the sum of the open-circuit voltages of both sub-cells. Subsequently a four-terminal device structure allowing for external series and parallel connection was developed using an electrically insulating optical spacer between the two metallic middle electrodes,[49] in order to resolve the problem of only being able to measure in series connection. Furthermore, three-terminal structures with a shared middle electrode have been proposed.[50,51]

As BHJ solar cells are processed from solution in a planar structure it is more pragmatic to connect the sub-cell in a tandem cell in series, which has been performed for various materials and material combinations, incorporating middle electrodes based on sputtered ITO,[52,53] metals and metal oxides deposited in vacuum.[54,55] Another breakthrough was realized by Gilot et al.[56] by achieving fully solution processed tandem devices using metal oxide layers processed from nanoparticles[56-58] or precursor[59,60] solutions. Also different device structures have been developed to avoid the problems encountered with stacking thin films on top of each other, like the combination of separate sub-cell devices with semitransparent contacts[61] or a folded tandem structure.[62]

In the remainder of this thesis we will consider a typical tandem device structure of two polymer:fullerene BHJ sub-cells utilizing zinc oxide (ZnO) and pH neutralized PEDOT:PSS as the connecting (semi-)transparent middle electrode, similar in design to the tandem cell as reported by Gilot et al.[56] and a tandem cell of 4.9 %,[63] showing the high potential of this middle electrode. Furthermore, the front sub-cell of a tandem solar cell is defined as the sub-cell nearest to the glass substrate, where the incident light passes through first. Similarly, the back sub-cell is the sub-cell furthest from the glass substrate, where the incident light passes through last.

1.9 Outline of this thesis

While organic solar cells have been studied intensely in the last decade and considerable effort has been spent in order to improve their performance, there is still ground for further improvement. One such way is the use of optical and electrical models in numerical simulations so as to understand where improvements in the device structure of organic solar cells is feasible. Underlying this thesis is the idea that a combination of an optical- and an electrical model can be used as a tool for the simulation of polymer:fullerene BHJ solar cells given certain specific parameters that adequately describe those solar cells from a theoretical standpoint.

As the optical model based on the transfer matrix formulation by Knittl forms the basis of this research, it will be discussed separately in chapter 2 of this thesis. It is an analytical model that assumes an effective medium approach with sharp boundaries for the layers in the organic photovoltaic device and except for some coherence conditions is entirely macroscopic in nature. The model provides a means to simulate the absorbed light intensity for any position inside the device calculated solely from the spectrum of the incident light and the optical parameters, thickness and placing of the materials that the layers of the device is comprised of.

In chapter 3 polymer:fullerene BHJ devices with poly(2-methoxy-5-(3',7'-dimethyl octyloxy)-*p*-phenylene vinylene) (MDMO-PPV) as polymer and PCBM as fullerene are investigated through experimental measurements and numerical simulations, in order to understand the influence of the unbalanced charge transport and the exciton generation profile in the active layer on the electrical performance of the device. We demonstrate that the electrical performance of thin (< 250 nm) devices does not change significantly when the exciton generation rate profile coming forth from optical simulations is replaced with an exciton generation rate profile that has a constant profile with the same total exciton generation rate. For thicker devices the simulated profile predicts higher electrical performance than with the constant profile, due to space charge limitations of the current density, which means that for more accurate electrical performance predictions, the optical model is needed to simulate a more realistic exciton generation profile.

When looking at polymer:fullerene devices with smaller band gaps, it is typically expected that the exciton generation rate and thus the charge generation rate is higher, which in combination with unbalanced charge transport should lead to an increase in space charge formation, hindering the extracted current density and overall electrical performance of the devices. In chapter 4 polymer:fullerene devices with varying polymer band gaps are simulated with help of optical and electrical modeling for balanced and unbalanced charge transport. We show, assuming an unchanging effective band gap, that the optical and electrical performance of a polymer:fullerene BHJ device do increase for decreasing band gap, going from 2.3 % to 4.1 % maximum *PCE*, but that its fill factor decreases for 250 nm from about 50 % to about 40% due to a one order of magnitude difference in the electron- and hole mobility. In such this demonstrates the higher space charge buildup for lower band gaps and its effect on the electrical performance of the device. If the unbalanced charge transport becomes balanced, an increase of maximum *PCE* from 4.1 % to 5.5 % is observed, showing that balancing charge transport is of more importance to the performance of small band gap polymer:fullerene BHJ solar cells than it is for high band gap ones.

Typical polymer:fullerene BHJ devices have a device structure such that most charge carriers are generated near the transparent anodes of the active layers, where electrons generally travel longer distances than holes. For so called inverted devices, where most charge carriers are generated near the transparent cathodes of the active layers, the holes generally travel longer distances than electrons. Under balanced transport conditions, both device structures are expected to have similar performance, yet for unbalanced charge transport, one of the two device structures should outperform the other due to difference in average distance that the slowest charge carrier has to travel to the electrode that extracts them. We will discuss the influence of that on buildup of space charge and its detrimental effects on device performance. In chapter 5 we demonstrate for modeled polymer:fullerene BHJ single and tandem cells that when holes are slower than electrons, that the normal device structure yields the best performance and in the reversed case of electrons being slower than holes, that the inverted structure yields the best performance. When electrons are ten times more mobile than holes, changing the structure from normal to inverted makes the *PCE* of a single cell with an active layer thickness of 250 nm drop from 7.5 % to 4.9 %. With holes being ten times as mobile as electrons, the structure's change from

inverted to normal decreases the *PCE* from 7.8 % to 4.7 %. Similar, yet less pronounced differences have been found when switching the device structure of tandem devices, when the device thicknesses are kept optimized.

In changing the polymer band gaps of single and tandem polymer:fullerene BHJ devices, the exciton generation rate as well as the effective band gap of the active layers can be tuned in such a way that the performance of such devices can be maximized. In past years optical and electrical modeling have been used to investigate what combinations of materials, polymer band gaps and active layer thicknesses yield the most optimized system with the highest device performance. We undertake such an investigation in chapter 5 for electrically optimized polymer:fullerene BHJ single and tandem devices that have variable polymer band gaps and active layer thicknesses. For the single device case a maximum *PCE* of 11.7 % is found, similar to earlier reports and usable as a reference. For the tandem cell case the maximum *PCE* is 14.1 %, again comparable to earlier reports, having the sub-cell with the smallest band gap placed closest to the reflecting electrode. As a result, optimized tandem devices are expected to improve on optimized single devices with an expected enhancement of about 20 – 25 %.

References

[1] U.S.Energy Information Administration, International Energy Outlook 2011, http://205.254.135.24/forecasts/ieo/, 2011.

[2] M. A. Green, K. Emery, Y. Hishikawa, and W. Warta, Prog. Photovoltaics **19**, 565 (2011).

[3] Technology Review, Mass Production of Plastic Solar Cells, http://www.technologyreview.com/energy/21574/page2/, 2008.

[4] C. K. Chiang, C. R. Fincher Jr., Y. W. Park, A. J. Heeger, H. Shirakawa, E. J. Louis, S. C. Gau, and A. G. MacDiarmid, Phys. Rev. Lett. **39**, 1098 (1977).

[5] K. M. Coakley and M. D. McGehee, Chem. Mater. **16**, 4533 (2004).

[6] J. Peet, A. J. Heeger, and G. C. Bazan, Acc. Chem. Res. **42**, 1700 (2009).

[7] H. Kallmann and M. Pope, J. Chem. Phys. **30**, 585 (1959).

[8] D. L. Morel, A. K. Gosh, T. Feng, E. L. Stogryn, P. E. Purwin, R. F. Shaw, and C. Fishman, Appl. Phys. Lett. **32**, 495 (1978).

[9] G. Chamberlain, Sol. Cells **8**, 47 (1983).

[10] G. Horowitz, Adv. Mater. **2**, 287 (1990).

[11] R. N. Marks, J. J. M. Halls, D. D. C. Bradley, R. H. Friend, and A. B. Holmes, J. Phys.: Condens. Matter **6**, 1379 (1994).

[12] C. W. Tang, Appl. Phys. Lett. **48**, 182 (1986).

[13] N. S. Sariciftci, L. Smilowitz, A. J. Heeger, and F. Wudl, Science **258**,1474 (1992).

[14] D. E. Markov, E. Amsterdam, P. W. M. Blom, A. B. Sieval, and J. C. Hummelen, J. Phys. Chem. A **109**, 5266 (2005).

[15] O. V. Mikhnenko, F. Cordella, A. B. Sieval, J. C. Hummelen, P. W. M. Blom, and M. A. Loi, J. Phys. Chem. B **112**, 11601 (2008).

[16] G. Yu, J. Gao, J. C. Hummelen, F. Wudl., and A. J. Heeger, Science **270**, 1789 (1995).

[17] S. A. Shaheen, C. J. Brabec, N. S. Sariciftci, F. Padinger, T. Fromherz, and J. C. Hummelen, Appl. Phys. Lett. **78**, 841 (2001).

[18] L. B. Schein, A. Rosenberg, and S. L. Rice, J. Appl. Phys. **60**, 4287 (1986).

[19] A. Peled and L. B. Schein, Chem.Phys. Lett. **153**, 422 (1988).

[20] L. B. Schein, A. Peled, and D. Glatz, J. Appl. Phys. **66**, 686 (1989).

[21] P. M. Borsenberger, L. Pautmeier, and H. Bässler, J. Chem. Phys. **94**, 5447 (1991).

[22] W. D. Gill, J. Appl. Phys. **43**, 5033 (1972).

[23] H. Bässler, Phys. Status Solidi B **175**, 15 (1993).

[24] S. V. Novikov, D. H. Dunlap, V. M. Kenkre, P. E. Parris, and A. V. Vannikov, Phys. Rev. Lett. **81**, 4472 (1998).

[25] L. Pautmeier, R. Richert, and H. Bässler, Synth. Met. **37**, 271 (1990).

[26] P. M. Borsenberger, T. Kung, and W. B. Vreeland, J. Appl. Phys. **68**, 4100 (1990).

[27] P. W. M. Blom, M. J. M. de Jong, and J. J. M. Vleggaar, Appl. Phys. Lett. **68**, 3308 (1996).

[28] M. A. Lampert and P. Mark, *Current injection in solids*, Academic Press New York, 1970.

[29] P. W. M. Blom, M. J. M. de Jong, and M. G. van Munster, Phys. Rev. B **55**, R656 (1997).

[30] P. W. M. Blom and M. C. J. M. Vissenberg, Mat. Sci. Eng. R **27**, 53 (2000).

[31] C.Tanase, P. W. M. Blom, and D. M. de Leeuw, Phys. Rev. B **70**, 193202 (2004).

[32] N. I. Craciun, J. Wildeman, and P. W. M. Blom, Phys. Rev. Lett. **100**, 056601 (2008).

[33] R. Coehoorn, W. F. Pasveer, P. A. Bobbert, and M. A. J. Michels, Phys. Rev. B **72**, 155206 (2005).

[34] V. D. Mihailetchi, L. J. A. Koster, J. C. Hummelen, and P. W. M. Blom, Phys. Rev. Lett. **93**, 216601 (2004).

[35] P. W. M. Blom, V. D. Mihailetchi, L. J. A. Koster, and D. E. Markov, Adv. Mater. **19**, 1551 (2007).
[36] Z. Knittl, *Optics of thin films*, John Wiley & Sons, 1976.
[37] L. A. A. Petterson, L. S. Roman, and O. Inganäs, J. Appl. Phys. **86**, 487 (1999).
[38] L. J. A. Koster, E. C. P. Smits, V. D. Mihailetchi, and P.W. M. Blom, Phys. Rev. B **72**, 085205 (2005).
[39] L. J. A. Koster, W. J. van Strien, W. J. E. Beek, and P. W. M. Blom, Adv. Funct. Mater. **17**, 1297 (2007).
[40] M. M. Mandoc, W. Veurman, L. J. A. Koster, B. de Boer, and P. W. M. Blom, Adv. Funct. Mater. **17**, 2167 (2007).
[41] D. Muhlbacher, M. Scharber, M. Morana, Z. Zhu, D. Waller, R. Gaudiana, and C. Brabec, Adv. Mater. **18**, 2884 (2006).
[42] M. M. Wienk, M. G. R. Turbiez, M. P. Struijk, M. Fonrodona, and R. A. J. Janssen, Appl. Phys. Lett. **88**, 153511 (2006).
[43] M. M. Wienk, M. Turbiez, J. Gilot, and R. A. J. Janssen, Adv. Mater. **20**,2556 (2008).
[44] R. Kroon, M. Lenes, J. C. Hummelen, P. W. M. Blom, and B. de Boer, Polym. Rev. **48**, 531 (2008).
[45] J. Hou, H Chen, S. Zhang, G. Li, and Y. Yang, J. Am. Chem. Soc. **130**, 16144 (2008).
[46] M. Hiramoto, M. Suezaki, and M. Yokoyama, Chem. Lett. **19**,327 (1990).
[47] A. Yakimov and S. R., Forrest, Appl. Phys. Lett. **80**, 1667 (2002).
[48] A. Hadipour, B. de Boer, J. Wildeman, F. B. Kooistra, J. C. Hummelen, M. G. R. Turbiez, M. M. Wienk, R. A. J. Janssen, and P. W. M. Blom, J. Appl. Phys. **16**, 1897 (2006).
[49] A. Hadipour, B. de Boer, and P. W. M. Blom, J. Appl. Phys. **102**, 074506 (2007).
[50] X. Guo, F. Liu, W. Yue, Z. Xie, Y. Geng, and L. Wang, Org. Electron. **10**, 1174 (2009).
[51] S. Sista, Z. Hong, M. Park, Z. Xu, and Y. Yang, Adv. Mater. **22**, E77 (2010).
[52] K. Kawano, N. Ito, T. Nishimori, and J. Sakai, Appl. Phys. Lett. **88**, 073514 (2006).
[53] J. Sakai, K. Kawano, T. Yamanari, T. Taima, Y. Yoshida, A. Fujii, and M. Ozaki, Sol. Energy Mater. Sol. Cells **94**, 376 (2010).
[54] D. W. Zhao, X. W. Sun, C. Y. Jiang, A. K. K. Kyaw, G. Q. Lo, and D. L. Kwong, Appl. Phys. Lett. **93**, 083305 (2008).
[55] X. Guo, F. Liu, B. Meng, Z. Xie, and L. Wang, Org. Electron. **11**, 1230 (2010).
[56] J. Gilot, M. M. Wienk, and R. A. J. Janssen, Appl. Phys. Lett. **90**, 143512 (2007).
[57] S. Sista, M. Park, Z. Hong, Y. Wu, J. Hou, W. L. Kwan, G. Li, and Y. Yang, Adv. Mater. **22**, 380 (2010).
[58] W. Chung, H. Lee, W. Lee, M. J. Ko, N. Park, B. Ju, and K. Kim, Org. Electron. **11**, 521 (2010).
[59] J. Y. Kim, K. Lee, N. E. Coates, D. Moses, T. Q. Nguyen, M. Dante, and A. J. Heeger, Science **317**, 222 (2007).
[60] Y. Chen, C. Yu, C. Chen, S. Chan, and C. Ting, J. Sol. Energy Eng. **132**, 021103 (2010).
[61] V. Shotriya, E. H. Wu, G. Li, Y. Yao, and Y. Yang, Appl. Phys. Lett. **88**, 064104 (2006).
[62] K. Tvingstedt, V. Andersson, F. Zhang, and O. Inganäs, Appl. Phys. Lett. **91**, 123514 (2007).
[63] J. Gilot, M. M. Wienk, and R. A. J. Janssen, Adv. Mater. **22**, E67 (2010).

Chapter 2

Transfer matrix model for organic solar cells

Summary

In this chapter we introduce the transfer matrix formalism describing the coherent passage of light through thin film layer stacks using elementary formulaic descriptions in 2 by 2 matrices. These are multipliable with each other and are used to calculate electric fields of light travelling in opposite directions in one position inside the layer stack denoted as a 1 by 2 electric field vector from another electric field vector in another position. First the basic equations governing propagation and refraction of plane light waves perpendicular to and in sunlight coherent thin layers are given. Then the transfer matrix model is introduced, including matrix multiplication, descriptions of transmission and reflection and propagation and refraction equations in matrix form. The incoherent model is derived for the incoherent description of the glass substrate and finally a brief step by step description of the numerical implementation of the combined optical model will be given.

2.1 Introduction

Successfully improving organic solar cells is a time consuming and therefore costly challenge. One way of reducing these costs is the use of accurate and descriptive models that enable fast and exhaustive numerical simulation of devices. Furthermore, such models can be used in order to exclude unfavorable parameter combinations for possible experimental devices and guide the search for new materials and techniques for improved designs. For organic solar cells the use of a well-defined optical model has become crucial in order to predict their performance and identify their strengths and weaknesses.

Optical models used in the past[1-6] are commonly based on the assumption of light decaying exponentially inside the stack of thin layers, and do not account for the expectable interference of light inside a structure that contains a highly reflective layer at the furthest end of the stack and that falls within the coherence length of sunlight ($\leq$ 50 μm).[7] In 1999 however, Petterson et *al.*[8] used the transfer matrix model developed by Knittl[9] to calculate the distribution of the intensity and absorption of light inside all layers of the thin film stack in order to predict the electrical performance of a polymer:fullerene bilayer device. Since then optical simulation of polymer solar cells has been increasingly based on the use of this model. Next to the determination of the internal quantum efficiency (IQE), which is the number of extracted charges per absorbed photon,[10] also the question whether an optical spacer enhances the light absorption in the active layer by redistributing light inside the device,[11,12] or the feasibility of a tandem structure has been addressed.[13-15]

In this thesis the transfer matrix model is used for the optical simulation of the various polymer:fullerene bulk heterojunction solar cells that are described in later chapters. It is based on the optical description of a stack of thin layers by the fundamental optical processes of propagation of planar light waves through lossy media and refraction of planar light waves at boundaries of neighboring media and utilizes vectors and matrices for a comprehensive and simple to use model. In order to have a full description of a BHJ device, including its glass substrate, an incoherent derivation of the transfer matrix model able to deal with incoherent light is

necessitated for the simulation in order to mathematically connect the glass substrate of the device, which is much thicker (0.6 – 0.75 mm) than the coherence of sunlight (≤ 50 μm), with the thin film layer stack, which is fully described by the transfer matrix model. First we list the necessary prerequisite assumptions for the coherent treatment of light in thin film layer stacks and then expound on the actual model of the optical description of planar light waves propagating through isotropic media and their refraction at boundaries between two neighboring media. After that the transfer matrix model is introduced and explained. Then the incoherent derivation of the transfer matrix model is explained and finally a total description of the optical processes and their numerical simulation is given.

2.2 Theoretical groundwork

When thin layers of material are illuminated, the refractions, reflections and absorption inside those films play a big role in determining the passage of light through such layers. Simple equations describe propagation through an isotropic medium and refraction at boundaries between two different media are sufficient for the description of multiple layers of thin films as found in organic solar cells. These equations are an integral part of the transfer matrix model, which is an elegant and concise way of optically describing multiple layer systems using matrices. A few assumptions are necessary in order to introduce these processes and equations and to use them in the transfer matrix model.

A: Maxwell's equations are the basis for all derived equations.
B: The layers are thinner than the coherence length of sunlight (≤ 50 μm).
C: The layers are perfectly flat and parallel to each other.
D: The boundary between any two neighboring layers is perfectly sharp.
E: The material in the layers is homogeneous and isotropic.
F: Light travels in planar waves.
G: Light interferes with itself in a quasi-static way.

With those assumptions in place, the only parameters needed for input of the basic equations of these processes and the transfer matrix model is the intensity of the incident light for all relevant wavelengths $I_0(\lambda)$, the light incidence angle θ, the complex refractive index for all relevant wavelengths of each layer $N_i(\lambda)$ and the thickness of each layer d_i. With those parameters known, the electric fields at any position in any layer can be calculated, as well as the resulting light intensity and light absorption. For simplicity's sake the incident light is taken to be perpendicular to the layer planes, thus $\theta = 0$.

2.3 Planar light wave propagation

When a planar light wave travels through an isotropic medium, its phase changes with the passage of time and distance traveled and decays exponentially along the travel direction if the medium is lossy

$$E(z,t) = e^{i\left(\frac{2\pi N}{\lambda}z - \frac{2\pi c}{\lambda}t\right)}E_0 \tag{2.1}$$

where E is the complex electric field at position z for time t, E_0 is the initial complex electric field and λ is the light's wavelength in vacuum. As the time variance of the electric field is irrelevant for the quasi-static nature assumed for light and the complex refractive index $N = n + ik$ consists of the refractive index n and the extinction coefficient k, equation 2.1 can be rewritten as

$$E(z) = e^{\frac{2\pi(k-in)z}{\lambda}}E_0 \tag{2.2}$$

This equation can be modified to get two equations governing the forward and backward propagation of light from one boundary of layer l through its material to the other boundary

$$E_l^{b+} = e^{\frac{-2\pi(k_l - in_l)d_l}{\lambda}} E_l^{f+} \tag{2.3a}$$

$$E_l^{b-} = e^{\frac{2\pi(k_l - in_l)d_l}{\lambda}} E_l^{f-} \tag{2.3b}$$

where E_l^{b+} and E_l^{b-} are the back electric fields of layer *l* propagating in the forward and backwards direction, where E_l^{f+} and E_l^{f-} are the front electric fields of layer *l* propagating in the forward and backwards direction, and d_l is the thickness of layer *l*. A schematic overview of the electric fields is given in Figure 2.1.

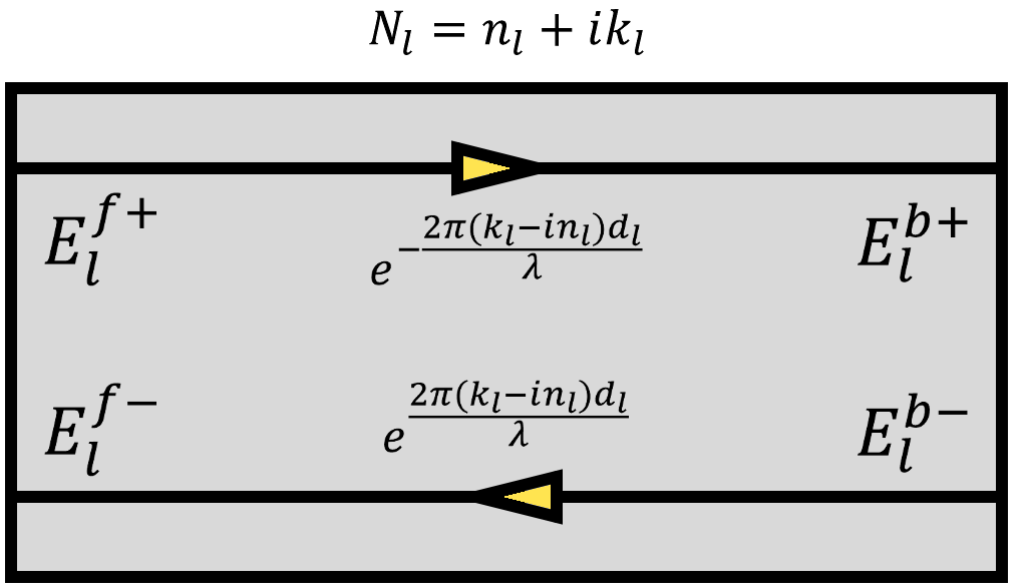

Figure 2.1: Schematic overview of light propagation through layer *l* in the layer stack. The different parameters are referred to in the text.

There is a different way of expressing the propagation of light through layer *l*, which is expressed in equations 2.4a+b:

$$E_l^{f+} = e^{\frac{2\pi(k_l - in_l)d_l}{\lambda}} E_l^{b+} \tag{2.4a}$$

$$E_l^{f-} = e^{\frac{-2\pi(k_l - in_l)d_l}{\lambda}} E_l^{b-} \tag{2.4b}$$

Here the front electric fields of layer l are calculated from the back electric fields, which is possible due to the assumption of quasi-static self-interference of light inside the layer stack. For calculation of light propagation inside a layer l where one of the electric field pairs is at position x and the other at either the layer's front or back boundary, it suffices to take an appropriate pair of formulae and replacing d_l with x.

2.4 Planar light wave refraction

When a planar wave passes from one medium to another medium through their shared flat boundary, part of it is transmitted from one to the other medium and the rest is reflected from the boundary, which is called refraction. For planar light waves having a direction of movement perpendicular to the boundary between layer l and m, the following two basic equations apply

$$E_l^{b+} + E_l^{b-} = E_m^{f+} + E_m^{f-} \tag{2.5a}$$

$$H_l^{b+} - H_l^{b-} = H_m^{f+} - H_m^{f-} \tag{2.5b}$$

where E and H denote the complex electric and magnetic field of the light wave respectively. By substitution, equation 2.5b can be reworked into

$$N_l E_l^{b+} - N_l E_l^{b-} = N_m E_m^{f+} - N_m E_m^{f-} \tag{2.6}$$

with $N_l = n_l + ik_l$ and $N_m = n_m + ik_m$. In Figure 2.2 a schematic overview of the electric fields in the two different materials is given.

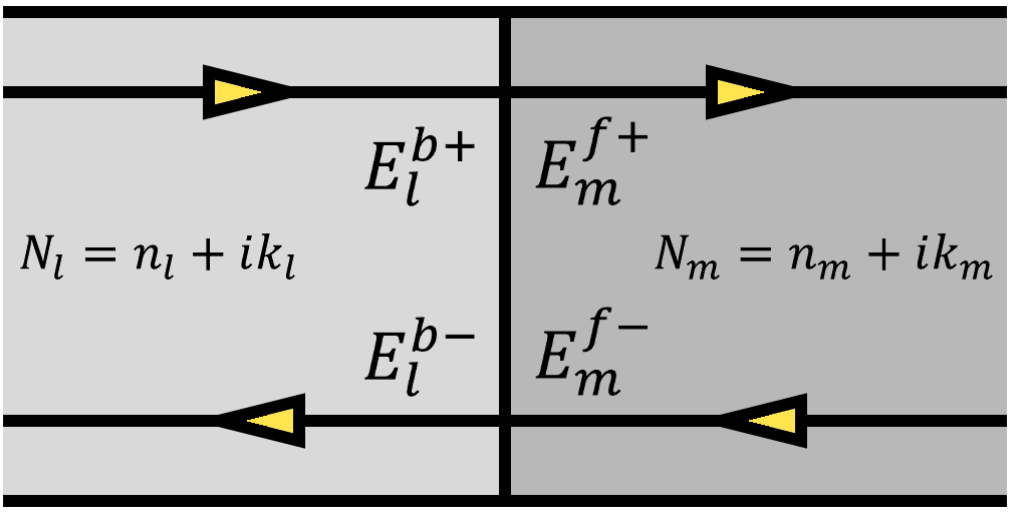

Figure 2.2: Schematic overview of light refraction at the boundary between layer *l* and layer *m* in the layer stack. The different parameters are referred to in the text.

With simple algebraic operations, equations 2.5a and 2.6 can be reworked into two equations that express the electric fields at the boundary in layer *m* as functions of the electric fields at the boundary in layer *l*

$$E_m^{f+} = \left(\frac{1}{2} + \frac{N_l}{2N_m}\right)E_l^{b+} + \left(\frac{1}{2} - \frac{N_l}{2N_m}\right)E_l^{b-} \qquad (2.7a)$$

$$E_m^{f-} = \left(\frac{1}{2} - \frac{N_l}{2N_m}\right)E_l^{b+} + \left(\frac{1}{2} + \frac{N_l}{2N_m}\right)E_l^{b-} \qquad (2.7b)$$

As can be seen, each of the two front electric fields in layer *m* are functions of both back electric fields in layer *l*. Similarly equations 2.5a and 2.6 can also be reworked into two equations that express the electric fields at the boundary in layer *l* as functions of the electric fields at the boundary in layer *m*

$$E_l^{b+} = \left(\frac{1}{2} + \frac{N_m}{2N_f}\right) E_m^{f+} + \left(\frac{1}{2} - \frac{N_m}{2N_f}\right) E_m^{f-} \tag{2.8a}$$

$$E_l^{b-} = \left(\frac{1}{2} - \frac{N_m}{2N_f}\right) E_m^{f+} + \left(\frac{1}{2} + \frac{N_m}{2N_f}\right) E_m^{f-} \tag{2.8b}$$

Similarly also each of the two front electric fields in layer *l* are functions of both back electric fields in layer *m*. The symmetry of equation 2.6 is reflected in the symmetry of equations 2.7a+b to equations 2.8a+b and this will be addressed again when discussing the transfer matrix model.

2.5 The transfer matrix model

The transfer matrix approach puts the equations established in paragraphs 2.3 and 2.4 in 2 by 2 matrices to transform the electric fields of forward and backward moving light in a part of the layer stack into those of light in a different location. This is accomplished by pairing the forward and backward propagating electric fields in 1 by 2 electric field vectors, which can then be multiplied with 2 by 2 matrices containing the appropriate equations in the right places to get the electric field vectors of the new location. The paired forward and backward electric fields are denoted as the complex 1 by 2 electric field vector $\vec{E} = \begin{bmatrix} E^+ \\ E^- \end{bmatrix}$, with E^+ being the forward field and E^- being the backward field. The general form of a 2 by 2 complex matrix *M* is given by equation 2.9

$$M = \begin{bmatrix} A & B \\ C & D \end{bmatrix} \tag{2.9}$$

where A, B, C and D are complex matrix multiplication elements. Yet this definition of the general matrix is insufficient, as there are two actual general matrix types possible, depending whether electric fields are calculated into the forward direction or into the backward direction. Let us assume two electric field vectors $\vec{E}_i$ and $\vec{E}_j$, with incoming light passing from $\vec{E}_i$ to $\vec{E}_j$ and reflected light passing in reverse. Then two matrices relate $\vec{E}_i$ and $\vec{E}_j$ between each other. One is the so called forward matrix M_{ij}^{+} and the other the backward matrix M_{ij}^{-}, their relationships with the electric field vectors given as equations 2.10a+b

$$\vec{E}_j = M_{ij}^{+}\vec{E}_i \tag{2.10a}$$

$$\vec{E}_i = M_{ij}^{-}\vec{E}_j \tag{2.10b}$$

As can be seen, the matrices are each other's inverse, leading to the following identity statement $M_{ij}^{+}M_{ij}^{-} = I_2 = M_{ij}^{-}M_{ij}^{+}$, where I_2 is the 2 by 2 identity matrix. Expressing both the electric field vectors and the transfer matrices in their full form we get the following expressions

$$\begin{bmatrix} E_j^{+} \\ E_j^{-} \end{bmatrix} = \begin{bmatrix} A_{ij}^{+} & B_{ij}^{+} \\ C_{ij}^{+} & D_{ij}^{+} \end{bmatrix} \begin{bmatrix} E_i^{+} \\ E_i^{-} \end{bmatrix} = \begin{bmatrix} A_{ij}^{+}E_i^{+} + B_{ij}^{+}E_i^{-} \\ C_{ij}^{+}E_i^{+} + D_{ij}^{+}E_i^{-} \end{bmatrix} \tag{2.11a}$$

$$\begin{bmatrix} E_i^{+} \\ E_i^{-} \end{bmatrix} = \begin{bmatrix} A_{ij}^{-} & B_{ij}^{-} \\ C_{ij}^{-} & D_{ij}^{-} \end{bmatrix} \begin{bmatrix} E_j^{+} \\ E_j^{-} \end{bmatrix} = \begin{bmatrix} A_{ij}^{-}E_j^{+} + B_{ij}^{-}E_j^{-} \\ C_{ij}^{-}E_j^{+} + D_{ij}^{-}E_j^{-} \end{bmatrix} \tag{2.11b}$$

As both equations can be treated in the same manner, we will do so and leave the choice of using either forward or backward matrices for calculations up to a choice of convenience. As such we will consider the general 2 by 2 matrix *M* and the general 1 by 2 vectors $\vec{E}_x$ and $\vec{E}_y$ in the following relation

$$\begin{bmatrix} E_y^+ \\ E_y^- \end{bmatrix} = \begin{bmatrix} A & B \\ C & D \end{bmatrix} \begin{bmatrix} E_x^+ \\ E_x^- \end{bmatrix} = \begin{bmatrix} AE_x^+ + BE_x^- \\ CE_x^+ + DE_x^- \end{bmatrix} \tag{2.12}$$

Within a coherent layers stack any amount of matrices can be multiplied with each other and can be used to calculate electric field pairs at any position from electric field pairs from any other position. Multiplication is performed as given by equation 2.13:

$$M_{a\to z}^T = M_{a,a+1} M_{a+1,a+2} M_{a+2,a+3} \cdots M_{z-3,z-2} M_{z-2,z-1} M_{z-1,z} \tag{2.13}$$

with $M_{a\to z}^T$ as the total multiplied matrix relating $\vec{E}_z = M_{a\to z}^T \vec{E}_a$ and each multiplied matrix $M_{q,q+1}$ relating $\vec{E}_{q+1} = M_{q,q+1}\vec{E}_q$. However, there are restrictions to the multiplication of transfer matrices, one being that all to be multiplied consequential matrices need to be neighboring and the other that all matrices need to be of the same type, either all forward matrices or all backward matrices.

When the appropriate matrices describing blocks of layers have been calculated from the matrices governing the individual layers, these can be used to directly calculate transmission, reflection and absorption properties of the layer blocks. It involves splitting equation 2.12 into the following 2 equations

$$E_y^+ = AE_x^+ + BE_x^- \tag{2.13a}$$

$$E_y^- = CE_x^+ + DE_x^- \tag{2.13b}$$

where $\vec{E}_x$ is the electric field vector at one end of the layer block and $\vec{E}_y$ is the electric field vector at the other end of the layer block. When considering transmission from *x* to *y* and reflection at the boundary of *x*, E_y^- is considered to be 0, as there is no *y* to *x* incident light involved for these kind of 'refraction' processes. This leads to the following expressions for *x* to *y* transmission and reflection coefficients

$$t_{xy} = \frac{AD - BC}{D} \tag{2.14a}$$

$$r_{xy} = -\frac{C}{D} \tag{2.14b}$$

where t_{xy} is the x to y transmission coefficient and r_{xy} is the x to y reflection coefficient. Similarly, y to x transmission and reflection have $E_x^+ = 0$, as these 'refraction' processes does not involve x to y incident light and the following expressions are found

$$t_{yx} = \frac{1}{D} \tag{2.15a}$$

$$r_{yx} = \frac{B}{D} \tag{2.15b}$$

with t_{yx} and r_{yx} being the y to x transmission and reflection coefficient respectively. The intensity of light I is expressed as

$$I = \frac{n|E|^2}{2Z_0} \tag{2.17}$$

where Z_0 is the impedance of absolute vacuum. With this equation the light intensity of each of the forward and backward traveling electric fields can be calculated as well as the total light intensity of the interfering electric fields, where the electric fields are added together as $\left|E^+ + E^-\right|^2$ and their complex nature automatically includes intensity interference. Integrating this equation with equations 2.14a+b and 2.15a+b gives the following four expressions

$$T_{xy} = \frac{n_y}{n_x}\left|\frac{AD - BC}{D}\right|^2 \tag{2.18a}$$

$$R_{xy} = \left|\frac{C}{D}\right|^2 \tag{2.18b}$$

$$T_{yx} = \frac{n_x}{n_y}\frac{1}{|D|^2} \tag{2.18c}$$

$$R_{yx} = \left|\frac{B}{D}\right|^2 \tag{2.18d}$$

where T_{xy} and R_{xy} are the x to y transmittance and reflectance respectively and T_{yx} and R_{yx} are the y to x transmittance and reflectance respectively. With these four equations the transmittance and reflectance of any composite block of layers can be calculated, including the whole layer stack. When the transmittance and reflectance of the layer stack are known, they can be used for integration with the incoherent optical model, which will be discussed later.

Planar light wave propagation can be expressed in two ways as a transfer matrix, one being the forward matrix and the other the backward matrix, which have been previously established. Equations 2.19a+b show both matrices

$$M_l^{prop+} = \begin{bmatrix} e^{\frac{-2\pi(k_l - in_l)z_l}{\lambda}} & 0 \\ 0 & e^{\frac{2\pi(k_l - in_l)z_l}{\lambda}} \end{bmatrix} \tag{2.19a}$$

$$M_l^{prop-} = \begin{bmatrix} e^{\frac{2\pi(k_l - in_l)z_l}{\lambda}} & 0 \\ 0 & e^{\frac{-2\pi(k_l - in_l)z_l}{\lambda}} \end{bmatrix} \tag{2.19b}$$

with M_l^{prop+} and M_l^{prop-} being the forward and backward propagation matrix for layer *l* respectively.

Similarly, planar light wave refraction can be expressed in the forward and backward matrix

$$M_{l,m}^{refr+} = \begin{bmatrix} \left(\frac{1}{2} + \frac{N_l}{2N_m}\right) & \left(\frac{1}{2} - \frac{N_l}{2N_m}\right) \\ \left(\frac{1}{2} - \frac{N_l}{2N_m}\right) & \left(\frac{1}{2} + \frac{N_l}{2N_m}\right) \end{bmatrix} \tag{2.20a}$$

$$M_{l,m}^{refr-} = \begin{bmatrix} \left(\frac{1}{2} + \frac{N_m}{2N_l}\right) & \left(\frac{1}{2} - \frac{N_m}{2N_l}\right) \\ \left(\frac{1}{2} - \frac{N_m}{2N_l}\right) & \left(\frac{1}{2} + \frac{N_m}{2N_l}\right) \end{bmatrix} \tag{2.20b}$$

with $M_{l,m}^{refr+}$ and $M_{l,m}^{refr-}$ being the forward and backward refraction matrix at the boundary between *l* and *m* respectively. Now the expressions used in these equations are equal if the layers *l* and *m* are normal for one equation and switched for the other, so these equations can be expressed in a more universal and direction-independent equation

$$M_{l\to m}^{refr} = \begin{bmatrix} \left(\frac{1}{2} + \frac{N_l}{2N_m}\right) & \left(\frac{1}{2} - \frac{N_l}{2N_m}\right) \\ \left(\frac{1}{2} - \frac{N_l}{2N_m}\right) & \left(\frac{1}{2} + \frac{N_l}{2N_m}\right) \end{bmatrix} \tag{2.21}$$

where $l \rightarrow m$ denotes the direction of the calculation. With these relations and their governing equations established, the incoherent model can be introduced.

2.6 The incoherent optical model

As the coherence length of sunlight (≤ 50 μm) is far smaller than the glass substrate's thickness (0.6 – 0.75 mm), the passage of light through the whole system has to be dealt in an incoherent fashion in addition to the coherent approach in the layer stack. The coherent structures of the combined glass substrate and layer stack need to be incorporated in the incoherent model and this is accomplished by calculating the transfer matrices of all coherent structures and the transmittances and reflectances of these structures and viewing the layer stack as an effective refractive boundary between glass and air. This accounts for the effective refraction properties of the whole layer stack between the glass substrate and the air behind it.With these transmittances and reflectances and the optical parameters of all incoherent materials the total transmittance T_T and reflectance R_T of the whole incoherent system can be calculated. These relate the incident light intensity I_I to the transmitted light intensity I_T and the reflected light intensity I_R

$$I_T = T_T I_I \tag{2.22a}$$

$$I_R = R_T I_I \tag{2.22b}$$

In the combined glass substrate and layer stack system, which is surrounded by air, there are only two coherent structures, the boundary between air and glass and the layer stack, which does incorporate glass and air. Figure 2.3 depicts a schematic overview of the incoherent transmission, reflection and propagation processes going on in the combined glass substrate and layer stack system.

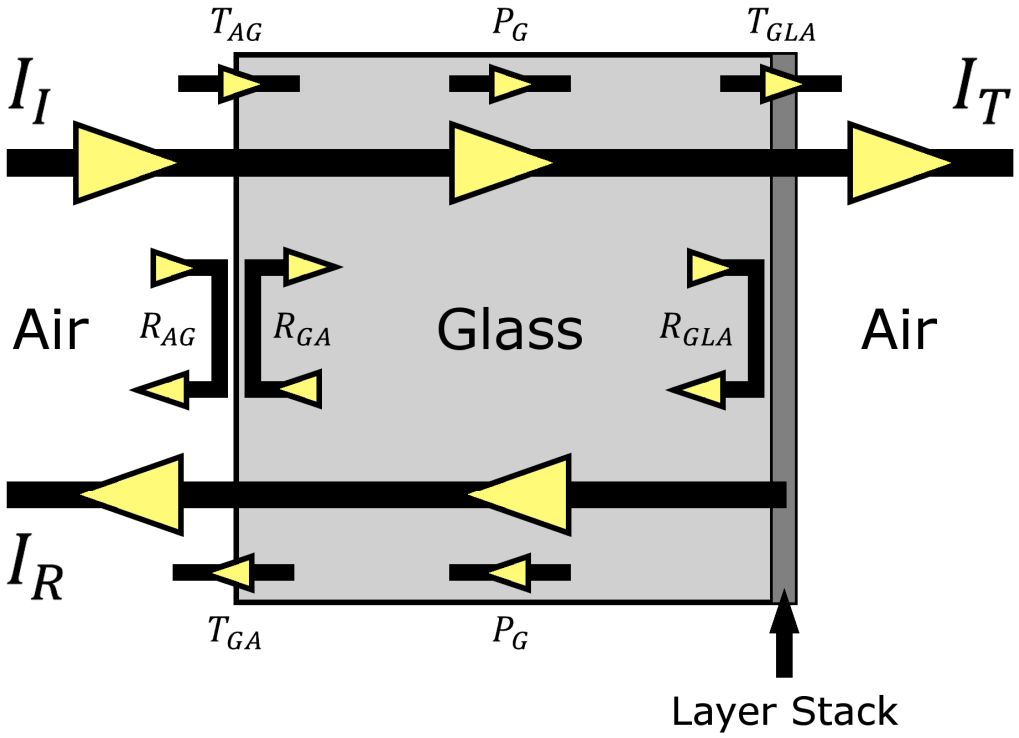

Figure 2.3: Schematic overview of light passage through the combined glass substrate and layer stack system. The different parameters are referred to in the text.

Here T_{AG} is transmittance from air to glass, R_{AG} is reflectance from air against glass, T_{GA} is transmittance from glass to air, R_{GA} is reflectance from glass against air, T_{GLA} is transmittance from glass through the layer stack to air, R_{GLA} is reflectance from glass against the layer stack and glass. The transmittances and reflectances are those of the transfer matrices of the air – glass boundary and layer stack. P_G describes the exponential decay of light propagating through the glass layer, which is an incoherent derivation of equation 2.2 and is expressed as

$$P_G = e^{\frac{-4\pi k_G z_G}{\lambda}} \tag{2.23}$$

where k_G is the extinction coefficient of glass and d_G is the thickness of the glass substrate. The total transmittance T_T is composed of transmittance through the air – glass interface T_{AG}, the subsequent light propagation of through the glass substrate P_G

as well as infinite reflection and propagation inside the glass and then the transmittance from glass through the layer stack to air T_{GLA}, which is given by

$$T_T = T_{AG} T_{GLA} P_G \sum_{n=0}^{\infty} (R_{GLA} R_{GA} P_G^2)^n = \frac{T_{AG} T_{GLA} P_G}{1 - R_{GLA} R_{GA} P_G^2} \tag{2.24}$$

As can be seen, the infinite progressing series can be expressed as a fraction. The total reflectance R_T is composed of reflectance from air against glass added to transmittance through the air – glass interface, propagation through the glass, reflectance from glass against the layer stack and air, propagation through the glass as well as infinite reflection and propagation inside the glass and then transmittance through the glass – air interface, which is given by

$$R_T = R_{AG} + T_{AG} R_{GLA} T_{GLA} P_G^2 \sum_{n=0}^{\infty} (R_{GLA} R_{GA} P_G^2)^n = R_{AG} \frac{T_{AG} R_{GLA} T_{GLA} P_G^2}{1 - R_{GLA} R_{GA} P_G^2} \tag{2.25}$$

With these equations the intensity of light can be calculated at all relevant sides of both boundaries of the glass substrate, where the light incident on the layer stack from the glass substrate is of interest, as it forms the connection between the incoherent model and the transfer layer approach.

2.7 Implementation in numerical simulation

With all necessary theoretical background discussed, there only rests the discussion of how the basic parameters of the AM 1.5 solar spectrum, the optical properties of the layers, their thickness and their order are used in order to calculate the photon absorption rate profile in the active layer, which is the basis for the active layer's exciton generation rate profile. We used a self-developed program called optically modeling layers in stacks [OMLIS] to perform these calculations. First, the backwards transfer matrices of all coherent subsystems are calculated, of the air –

glass boundary and of all layers and boundaries comprising the thin layer stack. Then the transfer matrices of the layer stack are multiplied to give two backwards matrices, one for the whole layer stack and one for a sub-stack from position *x* inside the active layer to the boundary between reflective metal electrode and air. The transfer matrices of the air – glass boundary and of the whole layer stack are used to calculate their relevant transmittances and reflectances, which with the light propagation formula (equation 2.23) and the AM 1.5 solar spectrum are used to calculate the light spectrum in the forward direction at the front of the layer stack. In conjuncture with equation 2.17 the forward electric field for each wavelength is calculated, with the assumption that each electric field only has a positive real component. Then using the transfer matrix of the whole layer stack and that of the designated sub-stack, the forward and backward electric fields at position *x* of the active layer are calculated, which with equation 2.17 yields the total light intensity of the interfering electric fields I_x at position *x*. Multiplying the light intensity with the absorption coefficient $\alpha = \frac{4\pi k}{\lambda}$ and dividing the result by the photon energy $\frac{hc}{\lambda}$ gives the photon absorption rate A_x at position *x*. Varying *x* across the active layer and integrating both I_x and A_x over the wavelength range gives both the light intensity profile and the photon absorption rate profile of the active layer. The latter is used as a basis for the exciton generation profile and in the rest of this thesis it is assumed that each absorbed photon generates exactly one exciton.

Programs like OMLIS are usable for more than just the calculation of light intensity and photon absorption rate profiles, they are also used for the calculation of transmission, reflection and absorption spectra, spectral analysis of the light intensity and photon absorption inside the active layer and calculation of the active layer's total photon absorption rate.

2.8 Summary

In this chapter, the transfer matrix model was introduced, which offers a coherent description of the optical processes inside a thin film layer stack. The basis of the model is that equations for the description of light propagation in a medium or light refraction at a boundary between two media can be adequately inserted in so called 2 by 2 transfer matrices, which can be multiplied with each other to yield simple 2 by 2 transfer matrices describing parts or the whole of the layer stack. The electric fields formed by light traveling forward and backward at one point in the stack can be put into a so called 1 by 2 electric field vector and the multiplied with the appropriate transfer matrix to yield a 1 by 2 vector describing the electric fields of forward and backward traveling light in any desired point in the layer stack.

First a list of required assumptions about the optical system was given to be able to introduce the coherent equations and the transfer matrix model, stressing the importance of the light traveling in plane waves perpendicular to the layers and with the layer stack and each layer being within sunlight coherency (≤ 50 μm). Then the equations used to describe coherent propagation of planar light waves in the medium of thin layers were introduced, after them the equations describing the refraction of planar light waves at the boundary between two neighboring layers. The general transfer matrix formalism was then explained, including the multiplication of matrices, formulaic descriptions for transmission and reflection and the previously established propagation and refraction equations. A derivation of the coherent model and the transmission and reflection described by the transfer matrix model was introduced to give an incoherent description of the transmission and reflection processes inherent to the glass substrate. Finally a brief step for step description of the numerical implementation of the combined optical model was given.

References

[1] A. K. Ghosh and T. Feng, J. Appl. Phys. **49**, 5982 (1978).

[2] J. Wagner, T. Fritz, and H. Böttner, Phys. Status Solidi A **136**, 423 (1993).

[3] A. Désormeaux, J. J. Max, and R. M. Leblanc, J. Phys. Chem. **97**, 6670 (1993).

[4] C. W. Tang, and A. C. Albrecht, J. Chem. Phys. **62**, 2139 (1975).

[5] A. K. Gosh, D. L. Morel, T. Feng, R. F. Shaw, and C. A. Rowe, Jr., J. Appl. Phys. **45**, 230 (1974).

[6] H. B. DeVore, Phys. Rev. **102**, 86 (1956).

[7] C. F. Bohren, E. Clothiaux, *Fundamentals of Atmospheric Radiation: An Introduction with 400 Problems*, John Wiley & Sons, 2006.

[8] L. A. A. Pettersson, L. S. Roman, and O. Inganäs, J. Appl. Phys. **86**, 487 (1999).

[9] Z. Knittl, *Optics of thin films*, John Wiley & Sons, 1976.

[10] L. H. Slooff, S. C. Veenstra, J. M. Kroon, D. J. D. Moet, J. Sweelssen, and M. M. Koetse, Appl. Phys. Lett. **90**, 143506 (2007).

[11] J. Y. Kim, S. H. Kim, H. H. Lee, K. Lee, W. L. Ma, X. Gong, and A. J. Heeger, Adv. Mater. **18**, 572 (2006).

[12] J. Gilot, I. Barbu, M. M. Wienk, and R. A. J. Janssen, Appl. Phys. Lett. **91**, 113520 (2007).

[13] W. Eerenstein, L. H. Slooff, S. C. Veenstra, and J. M. Kroon, Thin Solid Films **516**, 7188 (2008).

[14] G. Dennler, K. Forberich, T. Ameri, C. Waldauf, P. Denk, C. J. Brabec, K. Hingerl, and A. J. Heeger, J. Appl. Phys. **102**, 123109 (2007).

[15] V. Andersson, K. Tvingstedt, and O. Inganäs, J. Appl. Phys. **103**, 094520 (2008).

Chapter 3

Combined optical and electrical modeling of polymer:fullerene bulk heterojunction solar cells

Summary

Optical interference effects are important for the total absorption as well as the profile of the exciton generation rate in polymer:fullerene bulk heterojunction solar cells. For solar cells with an active layer of poly[2-methoxy-5-(3′,7′-dimethyloctyloxy)-1,4-phenylenevinylene] as electron donor and [6,6]-phenyl C_{61} butyric acid methyl ester as electron acceptor the total exciton generation rate can be directly extracted from the saturated photocurrent. It is demonstrated that for solar cells with an active layer thickness smaller than 250 nm a constant exciton generation profile, based on this extracted total rate, gives identical electrical characteristics as compared to exciton generation profiles from an optical model. For thicker cells interference effects have to be taken into account, since a uniform generation profile leads to an overestimation of recombination losses and space-charge formation.

3.1 Introduction

In recent years large progress has been made with regard to the understanding of the electrical device operation of polymer:fullerene BHJ solar cells, which in turn has paved the way to improved modeling and numerical simulation of such devices. As discussed in Chapter 1, dissociation of electron – hole (e – h) pairs at the donor/acceptor interface is an important process that can limit the charge generation efficiency.[1] A balanced transport of electrons and holes in the blend is needed to suppress the build-up of space-charge which, subsequently, will significantly reduce the power conversion efficiency.[2] Furthermore, the transport of electrons and holes in the blend needs to be enhanced in order to allow for fabrication of thicker films to maximize the absorption, without significant recombination losses.[3] Inclusion of the dissociation of bound electrons and holes at the donor/acceptor interface in a model based on the Poisson equation, current continuity equations and current equations (including both drift and diffusion), leads to a consistent description of the voltage and temperature dependence of the photocurrent of polymer:fullerene BHJ solar cells.[4] In this recently developed electrical model a constant profile has been assumed for the generation of excitons throughout the active layer.

Since a BHJ solar cell consists of a thin film layer stack of different materials on a transparent substrate it has been recognized that optical interference effects might play an important role in the performance of solar cells and thus the assumption of a constant generation profile could be inaccurate. For this reason, the transfer matrix model, as has been discussed in the previous chapter, has been developed initially for bi-layer devices,[5] and subsequently also for BHJ solar cells.[6,7] These model calculations demonstrated that for MDMO-PPV:PCBM BHJ solar cells an oscillatory behavior in the total absorption as a function of active layer thickness is expected from optical interference effects. Furthermore, the exact shape of the exciton generation profile shows a strong dependence on active layer thickness. Similar conclusions were found for solar cells with a BHJ of poly(3-hexylthiophene) (P3HT) and PCBM in a 1:1 weight ratio.[8,9] However, a coupling between optical effects and

solar cell parameters as short-circuit current J_{sc}, fill factor *FF* and layer thickness *L* is not straightforward. For MDMO-PPV:PCBM cells, for example, J_{sc} increases with increasing layer thickness due to an enhanced absorption, but the efficiency does not as a result of a decreasing *FF* due to space-charge formation and increased bimolecular recombination.[10] In order to incorporate optical effects in the solar cell performance, combined electrical and optical modeling has to be carried out. A first coupling between electrical and optical models has recently been made by Sievers et *al*.[11] They observed that interference effects, which affect the total exciton generation rate, do show up as an oscillatory behavior of J_{sc} as a function of active layer thickness. Similar findings were reported by Slooff et *al*. on BHJ solar cells based on a mixture of poly(9,9-didecanefluorene-alt-(bis-thienylene) benzothiadiazole) (PF10TBT) and PCBM in a 1:4 weight ratio.[12] On the other hand, the exciton generation profile had no significant influence on solar cell performance.[11] This is in contrast with the conclusion that electrical models using a constant generation profile are not appropriate to model solar cell characteristics.[8] We demonstrate that solar cells with active layer thicknesses smaller than 250 nm can be correctly modeled solely from electrical data, without having to incorporate optical modeling. The variation of the total exciton generation rate with layer thickness is experimentally available from the saturated photocurrent at high reverse bias. The average constant exciton generation rate based on this total rate gives identical simulation results as obtained with incorporation of the optically modeled exciton generation profiles.

3.2 Experimental methods

As a first step the electrical characteristics of MDMO-PPV:PCBM solar cells are investigated as a function of active layer thickness. The solar cells are made by spin-coating poly(3,4ethylenedioxythiophene)/poly(styrenesulfonic acid) (PEDOT:PSS) on top of a 0.6 mm thick glass substrate with patterned indium-tin-oxide (ITO) (140 nm) as a bottom contact. Subsequently, a blend of MDMO-PPV:PCBM (1:4 wt. ratio) with varying thickness is spin-coated on top in a nitrogen atmosphere. Finally, 0.5 nm

of lithium fluoride (LiF) covered with 80 nm aluminum (Al) is evaporated as top contact. The current density-voltage ($J - V$) characteristics of these devices were measured in a nitrogen atmosphere under illumination by a white light halogen lamp calibrated with a silicon photodiode to simulate the AM 1.5 global solar spectrum, which is the spectrum assumed for the numerical simulations.

For the optical modeling we used for the glass substrate, ITO electrode, and the MDMO-PPV:PCBM (1:4) blend the optical constants as reported by Hoppe et *al.*[13] The values for PEDOT:PSS and LiF were determined with variable angle ellipsometry using a Woollam VASE ellipsometer. For Al standard literature values were used.[14] An overview of the optical constants for the various layers is shown in Figure 3.1.

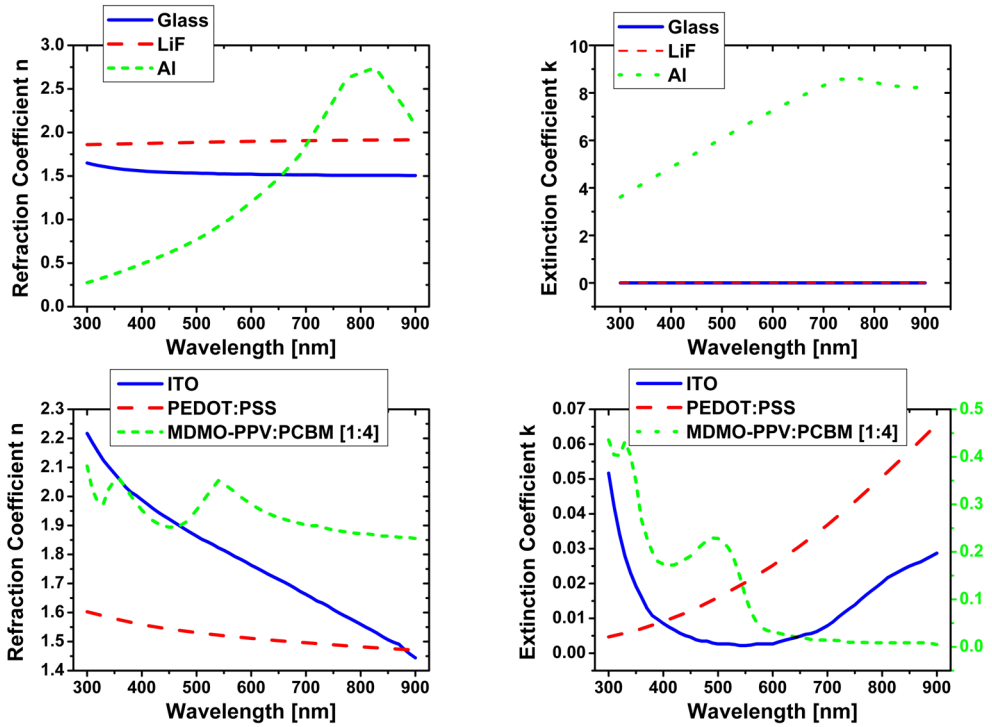

Figure 3.1: Optical parameters of glass, LiF, Al, ITO, PEDOT:PSS and MDMO-PPV:PCBM as a function of wavelength.

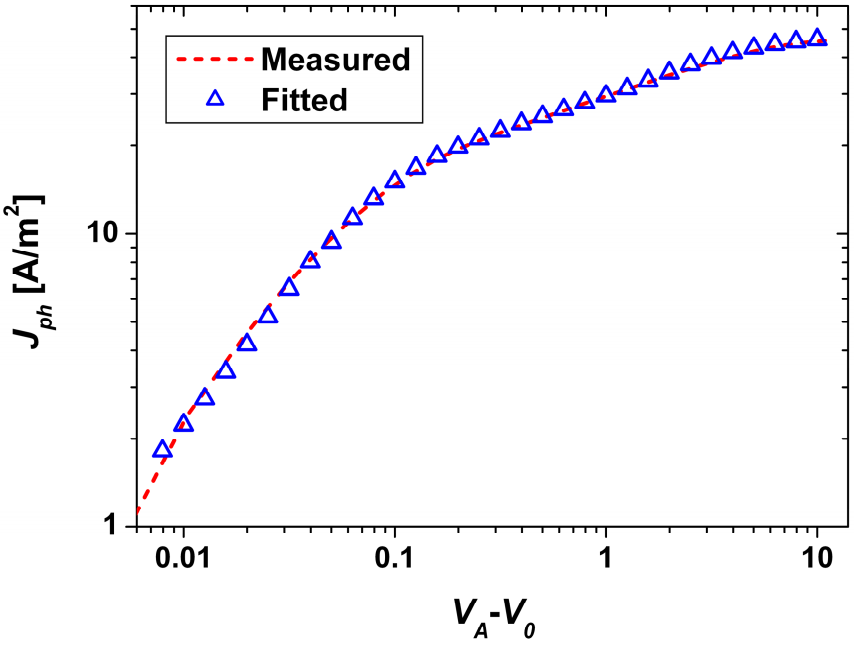

Figure 3.2: Measured (triangles) and simulated photo-current (dashed line) as a function of effective applied voltage (V_A - V_0) for a solar cell with an active layer thickness of 128 nm. Note that the photo-current at 10 V is near the saturated value.

3.3 Results

A. Saturated photocurrent

In Figure 3.2 the measured dependence of the photocurrent density J_{ph} on the effective applied voltage $V = V_A - V_0$, which is a measure of the net electric field in the cell,[1] is shown for an active layer thickness of 128 nm. Here V_A is the applied voltage and V_0 is the compensation voltage defined as $J_{ph}(V_A = V_0) = 0$. For V_A - V_0 up to 0.1 V we see a linearly increasing J_{ph}, resulting from the competition between drift and diffusion currents. For V_A - V_0 above 0.1 V J_{ph} tends to saturate as the slower increase of the drift-dominated current is limited by the maximum of the field-enhanced dissociation of the bound electron – hole (e – h) pairs that are formed after the

electron transfer from the donor to the acceptor.[1] At high reverse bias V_A - V_0 > 10 V all e – h pairs are dissociated and the photocurrent saturates to

$$J_{sat} = qG_{\max}L \tag{3.1}$$

where G_{max} is the maximum amount of bound e – h pairs that can be generated in the solar cell. It is evident that G_{max} is related to the total amount of absorbed light that governs the total exciton generation rate.

Also shown in Figure 3.2 as a dashed line are the modeled J_{ph} – V_A - V_0 characteristics using our recently developed numerical device model.[4] In this model it is assumed that photogenerated excitons dissociate into bound e – h pairs, which only partially dissociate into free charges. The amount of free charges that is generated can be described by

$$G(T,E) = G_{\max}P(T,E) \tag{3.2}$$

where P(*T,E*) is the probability of separation of bound e – h pairs at the donor/acceptor interface. The photogeneration of free charge carriers can be described by the geminate recombination theory of Onsager.[15] Furthermore, it was pointed out by Braun that the dissociation probability is influenced by the fact that the bound electron-hole pair has a finite lifetime.[16] The probability that a bound polaron pair dissociates into free charge carries at a given electric field *E* and temperature *T* is then given by:

$$P(T,E) = \frac{k_D(E)}{k_D(E) + k_F} \tag{3.3}$$

with k_F the rate constant that the bound electron-hole pair decays to its ground state, and $k_D(E)$ the rate constant for separation into free carriers, which is given by:[16]

$$k_D = k_R \frac{3}{4\pi a^3} e^{-E_B/kT} \left[1 + b + \frac{b^2}{3} + \frac{b^3}{18} + \frac{b^4}{180} + \ldots \right] \qquad (3.4)$$

with a the initial separation distance of the bound electron – hole pair at the interface, $b = e^3E/8\pi\varepsilon_0\varepsilon_r k^2T^2$, and E_B the binding energy of the electron – hole pair. Once separated, the charge carriers can again form a bound pair with a rate constant k_R. Using the Onsager theory for field dependent dissociation rate constants for weak electrolytes[17] for $k_D(E)$, Langevin recombination of free electrons and holes and a Gaussian distribution of donor-acceptor distances, the generation rate of producing free electrons and holes depends on the charge carrier mobilities μ_n and μ_p of the electron and holes respectively, the relative dielectric constant ε_r, the initial separation of e – h pairs a, and the ground state recombination rate k_F. As both the electric field distribution and the rate of charge separation are dependent on each other, an iterative algorithm and an educated guess on the initial values are needed. We use a program developed by L. J. A. Koster using such an algorithm based on the electrical model described here, which bases the initial value of the rate of charge separation on the total rate of exciton generation and assumes an uniform initial electric field.

As a next step the total rate of exciton generation is calculated using the optical model that what was introduced in the previous chapter following the transfer matrix approach developed by Knittl[18] and first utilized in organic photovoltaic devices by Petterson et *al*.[5] The calculated exciton generation rate is then transferred into a photocurrent J_{max} by assuming a 100 % internal quantum efficiency in the solar cell. In Figure 3.3 the experimentally determined J_{sat} is shown together with the calculated J_{max} as a function of solar cell active layer thickness L.

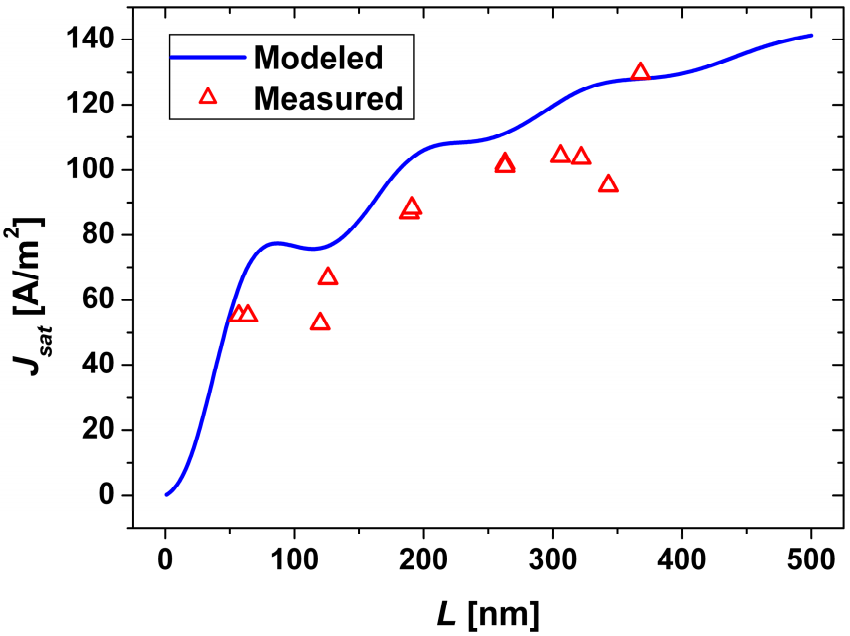

Figure 3.3: Experimental saturated photo-current J_{sat} (triangles) and theoretical maximum photo-current J_{max} (solid line) using the optically modeled total exciton generation rate and assuming a 100 % internal quantum efficiency.

As reported before, the calculated photocurrent following from the total exciton generation rate (J_{max}) increases in an oscillatory fashion with increasing active layer thickness, showing that the total exciton generation rate is influenced by the optical interference in the layer stack. We also observe that the experimental J_{sat} follows the trend of J_{max}, but it is typically about 90 % of its magnitude. This seems to indicate that of all created excitons about 90 % are effectively transferred into charge carriers at high reverse bias. The missing 10 % could be due to a combination of e – h pairs that are formed in 'dead-ends' of the phase separated morphology and limitations in charge transport. However, an alternative explanation could be that our materials have slightly different optical constants as compared to the reported values that we use in our calculations.[6] This could lead to a slight overestimation of the calculated absorption and is a subject of further study.

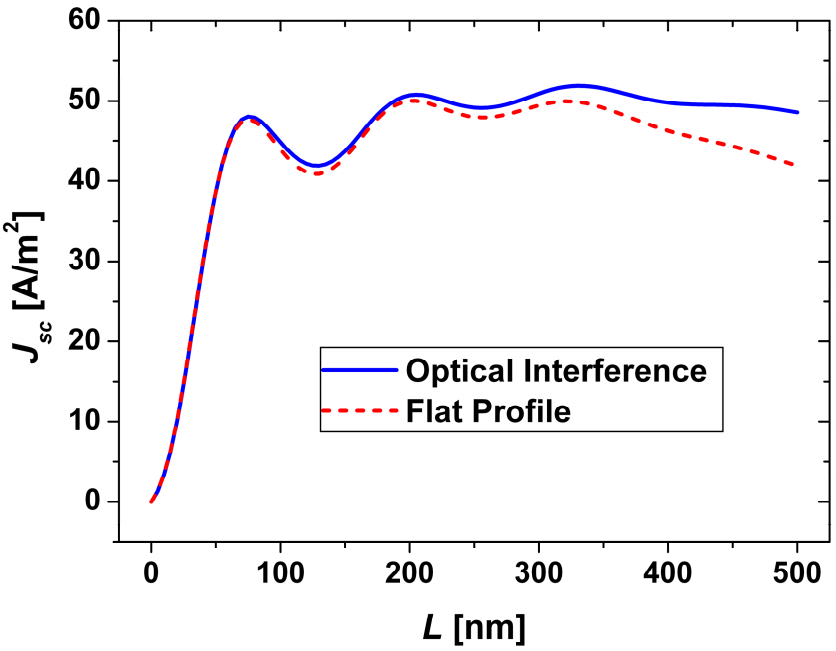

Figure 3.4: Simulated short-circuit currents using the calculated exciton generation rate profile $J_{sc}^{Profile}$ (solid line) or a constant average profile $J_{sc}^{Average}$ (dashed line) as a function of active layer thickness under 1000 W/m^2 AM 1.5 illumination.

B. Influence of optical interference

Subsequently, the calculated exciton generation profiles are used as input for the electrical device model. The result is shown in Figure 3.4 where the short-circuit current using the exciton generation rate profiles is shown ($J_{sc}^{Profile}$), together with the short-circuit current using an average exciton generation rate ($J_{sc}^{Average}$). The average exciton generation rate was chosen such that the total amount of generated excitons is identical to the amount of generated excitons for the profile. It is clear that for active layer thicknesses up to 250 nm the calculated $J_{sc}^{Profile}$ and $J_{sc}^{Average}$ are identical, as has also been reported by Sievers et *al.*, who calculated the J_{sc} up to layer thicknesses of 275 nm.[11] For layer thicknesses exceeding 300 nm we observe that $J_{sc}^{Profile}$ and $J_{sc}^{Average}$ clearly start to diverge. Thus, for solar cells with active layer thicknesses up to 275 nm the use of a constant exciton generation profile is justified for simulating

the performance of MDMO-PPV:PCBM based solar cells. The variation of the total exciton generation rate with layer thickness due to optical interference is taken into account by using the experimental J_{sat} as a measure for the total exciton generation rate.

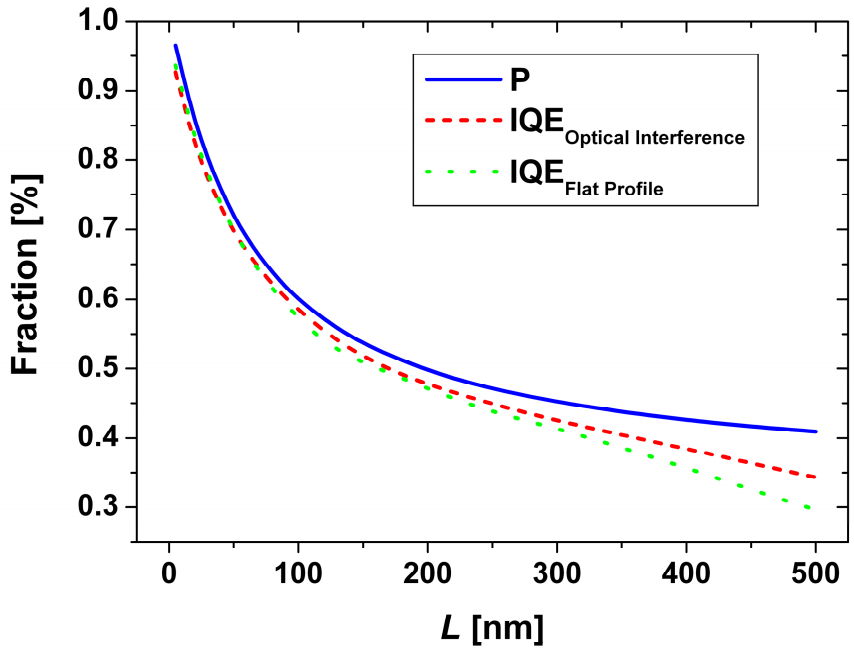

Figure 3.5: Average electron-hole pair dissociation probability $P(E,T)$ (solid line) and internal quantum efficiency at zero bias for the exciton generation rate profile $IQE_{sc}^{Profile}$ (dashed line) and the uniform profile $IQE_{sc}^{Average}$ (dotted line) as a function of active layer thickness.

Another interesting observation is that the calculated short-circuit currents follow the oscillatory behavior of the total absorption, but they do not further increase with increasing layer thickness. In Figure 3.5 $J_{sc}^{Profile}/J_{max}$ and $J_{sc}^{Average}/J_{max}$, representing the internal quantum efficiency (IQE) under short-circuit condition, are plotted as a function of active layer thickness L. The internal quantum efficiency strongly decreases with increasing layer thickness. As stated above, the dissociation of bound e – h pairs is an important process in MDMO-PPV:PCBM BHJ solar cells.

In Figure 3.5 the dissociation efficiency $P(E,T)$ is also shown at an electric field of V_{oc}/L as a function of L. By increasing the active layer thickness the electric field at short-circuit, typically given by V_{oc}/L with V_{oc} the open-circuit voltage, is reduced, thereby reducing $P(E,T)$. Apart from that, as stated above the dissociation efficiency also depends on the initial separation distance a (1.2 nm) of the bound electron and hole, and the decay rate k_f (10^6 s^{-1}) of the bound e – h pair. Both have been determined from the voltage and temperature dependence of the photocurrent under reverse bias.[1] The agreement between $P(E,T)$ and IQE shows that the reduced e – h dissociation efficiency is the main origin for the reduction of J_{sc} for thick samples. The increasing difference between $P(E,T)$ and IQE for thick samples is a result of increasing recombination losses and a build-up of space charge.[10] For a 100 nm device the bimolecular recombination losses only amount to a few percent.[4]

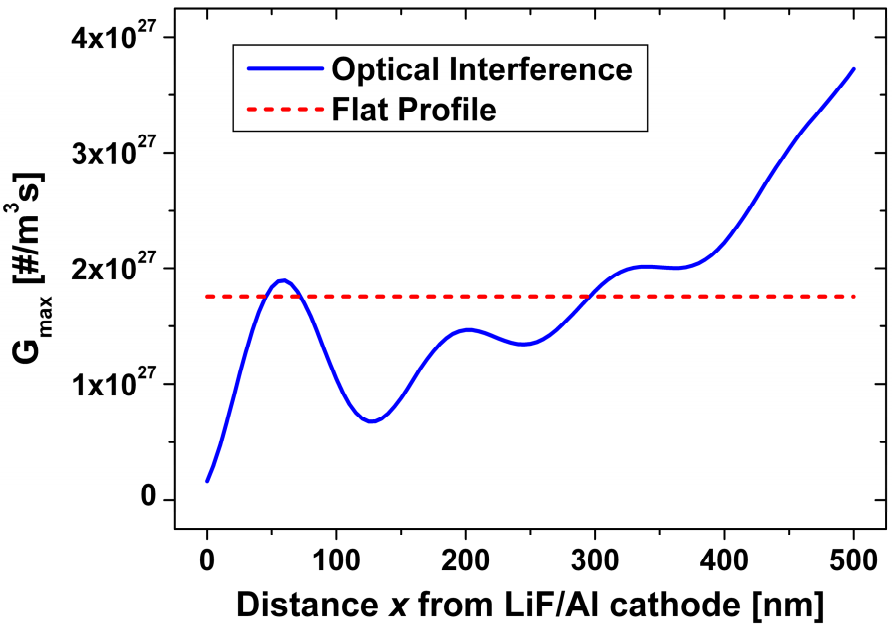

Figure 3.6: Simulated exciton generation rate profile (solid line) and its average (dashed line) as a function of distance x from the LiF/Al/ cathode. Note the higher exciton generation rate near the anode (x = 500 nm) for the exciton generation rate profile.

C. Space charge and active layer thickness

In Figure 3.4 it also appears that for thicknesses larger than 275 nm the $J_{sc}^{Profile}$ is lower than $J_{sc}^{Average}$, and that their difference increases with increasing thickness. In order to evaluate this difference we plot in Figure 3.6 the exciton generation rate profile and its average as a function of distance x from the LiF/Al electrode for a 500 nm thick active layer. It appears that relatively more excitons are generated near the PEDOT:PSS anode for the exciton generation profile as compared with its average. So in the case of the generation profile, the holes, which have a lower mobility than the electrons, are created close to the contact where they are extracted. This will reduce the amount of holes that are lost during transport due to bimolecular recombination and thus will enhance the efficiency. Furthermore, the build-up of space charge will be less in case the exciton generation profile is taken as initial distribution.

To demonstrate this reduction of space charge, we simulated the photocurrent for both the exciton generation rate profile and its average as a function of V_A - V_0 for a 500 nm thick active layer, as shown in Figure 3.7. This shows that the build-up of space charge is less severe for the exciton generation rate profile than for its average.

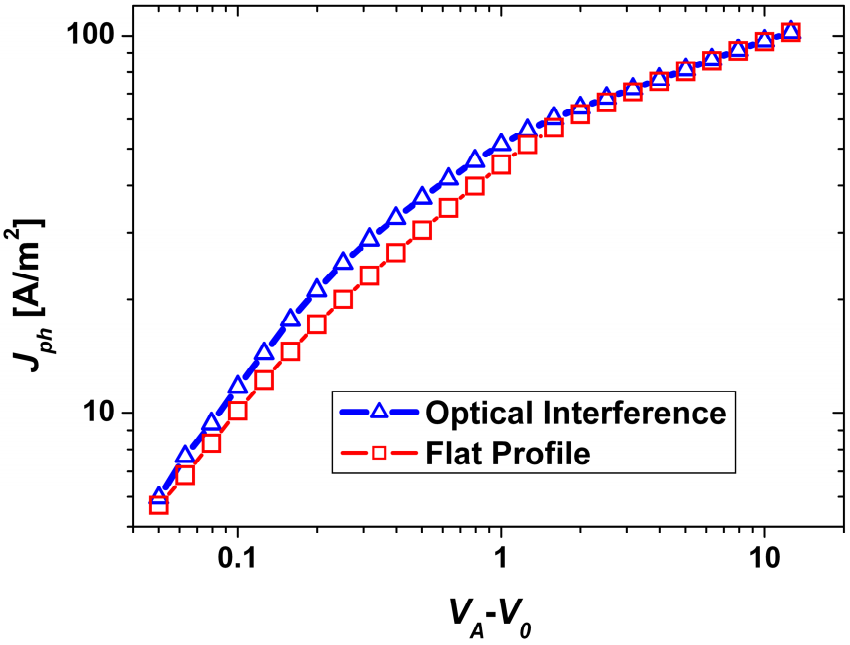

Figure 3.7: Photocurrent J_{ph} as a function of effective voltage V_A - V_0 for the exciton generation rate profile (triangles with solid line) and its average (squares with dashed line) for an active layer thickness of 500nm.

3.4 Conclusions

In conclusion, we have shown that the average exciton generation rate of MDMO:PCBM devices can be experimentally extracted from the saturated photocurrent at high reverse bias. For MDMO:PCBM devices under these conditions the total amount of generated excitons is close to the total amount of extracted charges. The variation of the total exciton generation rate with active layer thickness due to interference is then automatically taken into account. The device operation parameters, J_{ph}, J_{sc} and *IQE*, for solar cells with active layers thinner than 250 nm show no significant difference when either an exciton profile as obtained from optical modeling is used or a constant exciton generation rate profile, provided that the total exciton generation rate of both profiles are the same. For devices with active layers thicker than 300 nm it is important to include the optical exciton generation profiles. The losses due to bimolecular recombination and space-charge formation become

both dependent on the initial position of the slowest carrier, which are holes in the case of MDMO:PCBM devices.

References

[1] V. D. Mihailetchi, L. J. A. Koster, J. C. Hummelen, and P. W. M. Blom, Phys. Rev. Lett. **93**, 216601 (2004).
[2] V. D. Mihailetchi, L. J. A. Koster, J. C. Hummelen, and P. W. M. Blom, Phys. Rev. Lett. **94**, 126602 (2005).
[3] M. M. Mandoc, L. J. A. Koster, and P. W. M. Blom, Appl. Phys. Lett. **90**, 133504 (2007).
[4] L. J. A. Koster, E. C. P. Smits, V. D. Mihailetchi, and P. W. M. Blom, Phys. Rev. B **72**, 085205 (2005).
[5] A. A. Petterson, L.S. Roman, and O. Inganäs, J. Appl. Phys. **86**, 487 (1999).
[6] H. Hoppe, N. Arnold, N. S. Sariciftci, and D. Meissner, Sol. En. Mat. & Sol. Cel. **80**, 105 (2003).
[7] N.-K. Persson, H. Arwin, and O. Inganas, J. Appl. Phys. **97**, 034503 (2005).
[8] A. J. Moulé, J. B. Bonekamp, and K. Meerholz, J. Appl. Phys. **100**, 094503 (2006).
[9] H. Hoppe, S. Shokhovets, and G. Gobsch, Phys. Stat. Sol. **1**, 40 (2007).
[10] M. Lenes, L. J. A. Koster, V. D. Mihailetchi and P.W.M. Blom, Appl. Phys. Lett. **88**, 243502 (2006).
[11] D. W. Sievers, V. Shrotriya, and Y. Yang, J. Appl. Phys. **100**, 114509 (2006).
[12] L. H. Slooff, S. C. Veenstra, J. M. Kroon, D. J. D. Moet, J. Sweelssen, and M. M. Koetse, Appl. Phys. Lett. **90**, 143506 (2007).
[13] H. Hoppe, N. S. Sariciftci, D. Meissner, Mol. Cryst. Liq. Cryst. Sci. Technol., Sect. A **385** , 113 (2002).
[14] D. R. Lide, *Handbook of Chemistry and Physics* (CRC, Boca Raton 1994).
[15] L. Onsager, Phys. Rev. **54**, 554 (1938).
[16] C. L. Braun, J. Chem. Phys. **80**, 4157 (1984).
[17] L. Onsager, J. Phys. Chem. **2**, 599 (1934).
[18] Z. Knittl, *Optics of Thin Films* (Wiley, London 1976).

Chapter 4

Role of the balanced charge carrier transport in low band gap polymer:fullerene bulk heterojunction solar cells

Summary

Lowering of the optical band gap of conjugated polymers in bulk heterojunction solar cells not only leads to an increased absorption but also to an increase of the optimal active layer thickness due to interference effects at longer wavelengths. The increased carrier densities due to the enhanced absorption and thicker active layers make low band gap solar cells more sensitive to formation of space-charges and recombination. By systematically red-shifting the optical parameters of poly[2-methoxy-5-(3',7'-dimethyloctyloxy)-*p*-phenylenevinylene] (MDMO-PPV) and 6,6-phenyl C_{61}-butyric acid methyl ester (PCBM) we simulate the effect of a reduced band gap on the solar cell efficiencies. We show that especially the fill factor of low band gap cells is very sensitive to the balance of the charge transport. For a low band gap cell with an active layer thickness of 250 nm the fill factor of 50% for balanced transport is reduced to less than 40% by an imbalance of only one order of magnitude.

4.1 Introduction

The efficiency of organic polymer:fullerene bulk heterojunction solar cell performance has been steadily increasing in the last years, going from 2.5 % efficiency in 2001[1] to 3.5 % in 2003[2], up to 5.5 % in 2007[3,4], and recently an efficiency of 8,3% has been reported.[5] Part of the improvement originated from the refinement of existing production techniques to optimize the active layer morphology[6-8]. The majority of the improvement, however, came from the development of low band gap polymers.[3,4,9-17] By decreasing the band gap of the donor the amount of absorbed photon flux increases due to an enhanced overlap with the solar spectrum. A lowering of the polymer band gap can either be achieved by a lowering of the lowest unoccupied molecular orbital (LUMO) or by a raise of the highest occupied molecular orbital (HOMO). The lowering of the LUMO is limited by the energy offset needed for electron transfer to the acceptor, typically 0.4 eV. A raise of the HOMO on the other hand will lead to a decrease of the open-circuit voltage V_{oc}. A theoretical study by Koster *et al.*[18] showed that a decrease of the band gap from 2.1 eV to 1.5 eV by lowering the lowest unoccupied molecular orbital (LUMO) and keeping the highest occupied molecular orbital (HOMO) in place is expected to result in a power conversion efficiency η increase from 3.5 % to over 8 %. This enhanced performance mainly originated from an increased short-circuit current density J_{sc} due to an increased absorption. However, an increased absorption is accompanied by an enhanced carrier density in the solar cell and thus also to an increase of the bimolecular recombination. Furthermore, the higher carrier densities make the solar cells also more sensitive for the buildup of space-charge, caused by an imbalanced charge transport. Space-charge buildup is also dependent on the absorption profiles in the solar cell, which were not included in these calculations. To obtain more insight in the operation of low band gap solar cells combined optical and electrical modeling is required to address the role of the absorption profiles for wide and small band gap polymer:fullerene solar cells, as well as the role of unbalanced charge transport and a high recombination rate. In this chapter we discuss simulations

of polymer:fullerene solar cells by systematically varying the polymer band gap. We compare wide and small band gap polymer:fullerene bulk heterojunction solar cells with both unbalanced transport, where the hole mobility is an order of magnitude less than the electron mobility, and balanced transport with equal electron and hole mobilities.

4.2 Electrical and optical parameters

As a model system we have chosen a blend of poly[2-methoxy-5-(3',7'-dimethyloctyloxy)-*p*-phenylenevinylene] (MDMO-PPV) and 6,6-phenyl C_{61}-butyric acid methyl ester (PCBM) in a weight ratio of 1 to 4. In order to systematically simulate the effect of the band gap the optical parameters of MDMO-PPV are red-shifted in energy from 0 to 0.8 eV in steps of 0.2 eV, such that the LUMO lowered while the HOMO is kept constant, to preserve the energy gap between the HOMO of the polymer and the LUMO of the PCBM and thus to preserve V_{oc}. The electron mobility μ_e of the PCBM is set to 2×10^{-7} m^2/Vs,[19] whereas the hole mobility μ_h is varied between 2×10^{-8} m^2/Vs[20] for the unequal mobility case and 2×10^{-7} m^2/Vs for balanced transport. All other optical and electrical parameters are equal to those of MDMO-PPV and are kept constant in the simulations. For a complete solar cell we consider a glass substrate with a stack of thin layers on top of it: first 140 nm of indium tin oxide (ITO) as electrical contact, 50 nm of poly(3,4ethylenedioxythiophene)/poly(styrenesulfonic acid) (PEDOT:PSS) as anode, 10 to 500 nm of polymer:PCBM [1:4] as active layer, 0.5 nm of lithium fluoride (LiF) as electron injection layer and 80 nm of aluminum (Al) as reflecting cathode. As optical model we use the transfer matrix formalism[21] as described in Chapter 2. The electrical modeling is based on a numerical device model[22] as discussed in Chapter 1. The optical model is used to calculate the photonic absorption rate profile inside the active layer using the AM 1.5 solar spectrum and the thickness and optical parameters of the various materials. Assuming 100 % conversion efficiency from absorbed photons to excitons to bound electron-hole pairs, the electrical model is used to calculate the electrical behavior of the solar cell. As optical parameters the complex

refractive indices of the materials are used, where the values of PEDOT:PSS were reported by Petterson *et al.*[21], those of PCBM by Hoppe *et al.*[23] and those of Al were taken from literature.[24] The values of the remaining materials, glass, ITO, MDMO-PPV and LiF were determined with variable angle ellipsometry using a Woollam VASE ellipsometer. Figure 4.1 shows the *n* (solid lines) and *k* (dashed lines) as a function of λ from 300 to 1500 nm for PCBM, MDMO-PPV and four of its red-shifted variants with red-shifts of 0.2 to 0.8 eV in steps of 0.2 eV. It should be noted that red-shifting the optical parameters in equal energy parts translates into a larger shift in wavelength and a broadening of the spectral features, resulting in a higher photonic absorption rate. The optical properties of the polymer:PCBM blend are comprised of 20 % and 80 % of the optical properties of the red-shifted MDMO-PPV polymer and PCBM.

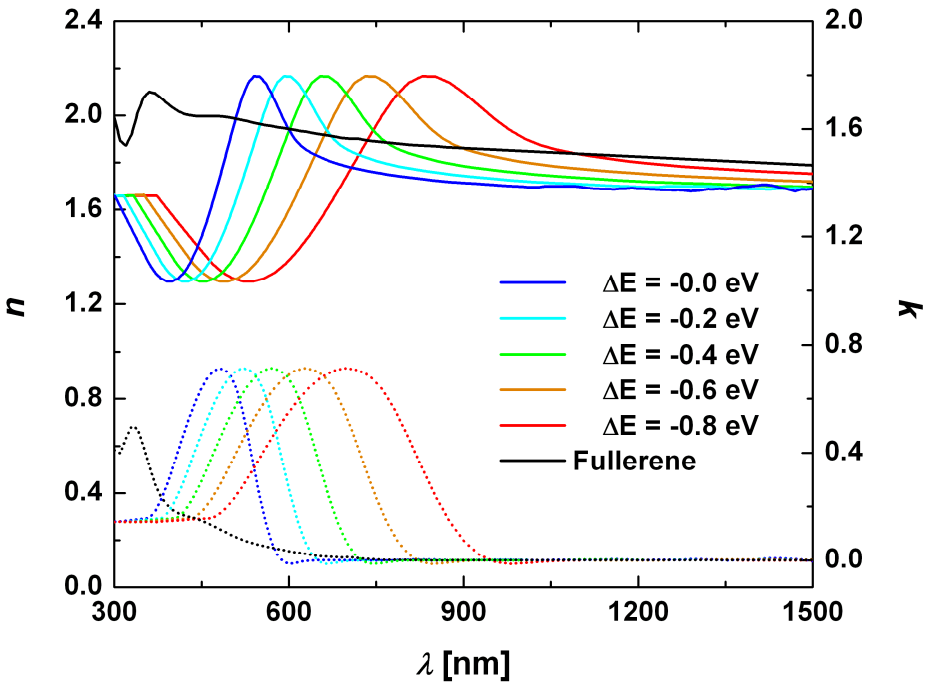

Figure 4.1: Optical parameters of PCBM and MDMO-PPV and 4 red-shifted variants as a function of wavelength λ.

4.3 Organic solar cells

Using the thicknesses and optical parameters of the materials provided previously and the transfer matrix formalism, the light intensity distribution inside the active layer can be calculated and with it the photon absorption rate as a function of position in the active layer. With the electrical parameters of the blend as described by Lenes *et al.*[25], we calculate the short-circuit current J_{sc}, the fill factor *FF* and η of the solar cells. Figure 4.2 shows J_{sc} as a function of active layer thickness L for a band gap shift ΔE from 0 to 0.8 eV in steps of 0.2 eV using an electron mobility μ_e of 2 x 10^{-7} m^2/Vs and a hole mobility μ_h of 2 x 10^{-8} m^2/Vs.[19,20]

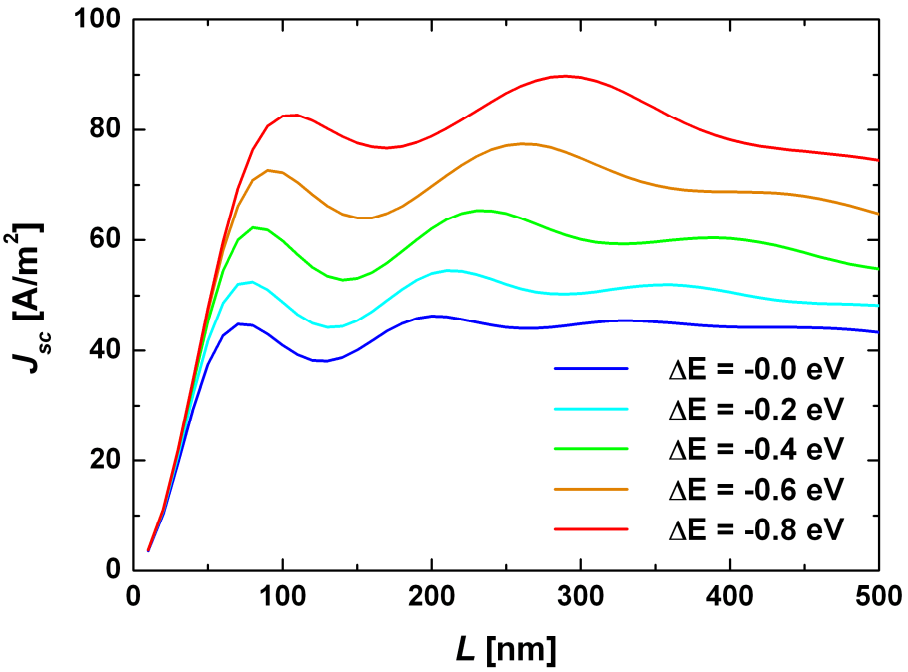

Figure 4.2: Short-circuit current density J_{sc} as a function of active layer thickness L for red-shift ΔE from 0 to 0.8 eV using μ_h = 2 x 10^{-8} m^2/Vs and μ_e = 2 x 10^{-7} m^2/Vs.

It is immediately clear that J_{sc} increases for increasing ΔE, due to a better overlap between absorption spectrum and solar spectrum. Typically, at the optimum layer

thickness J_{sc} increases from 44.8 to 82.7 A/m^2, representing a near doubling for a band gap shift from 2.4 eV to 1.6 eV. For very thin active layers (< 50 nm), the increase in J_{sc} due to the band gap lowering increase is diminished due to destructive interference between incident and reflected light near the cathode, thereby decreasing the total light irradiance. The interference caused by the aluminum cathode also leads to an oscillatory behavior of the light absorption and thus J_{sc} on the active layer thickness. As photons with longer λ are absorbed for increasing ΔE, the interference patterns for those photons will have longer oscillatory periods for the internal absorption rate profiles and as a result the oscillatory features of J_{sc} shift to higher layer thickness, as observed in figure 4.2. Quantitatively, for increasing ΔE from 0 to 0.8 eV, the optimum layer thickness increases from 70 to 110 nm.

As a next step the efficiency η is calculated as a function of the red-shifting of the polymer absorption spectrum. Figure 4.3 shows η as a function of L for ΔE from 0 to 0.8 eV in steps of 0.2 eV, using μ_e and μ_h of 2 x 10^{-7} m^2/Vs and 2 x 10^{-8} m^2/Vs respectively. With increasing ΔE again the optimum layer thickness increases from 70 to 100 nm due to interference effect. The absolute value of η increases from 2.3 to 4.1 % respectively, which is a near doubling in η. A difference with J_{sc} is that η increases to a clear maximum and then decreases for increasing active layer thickness, indicating extra losses for increasingly thick layers.

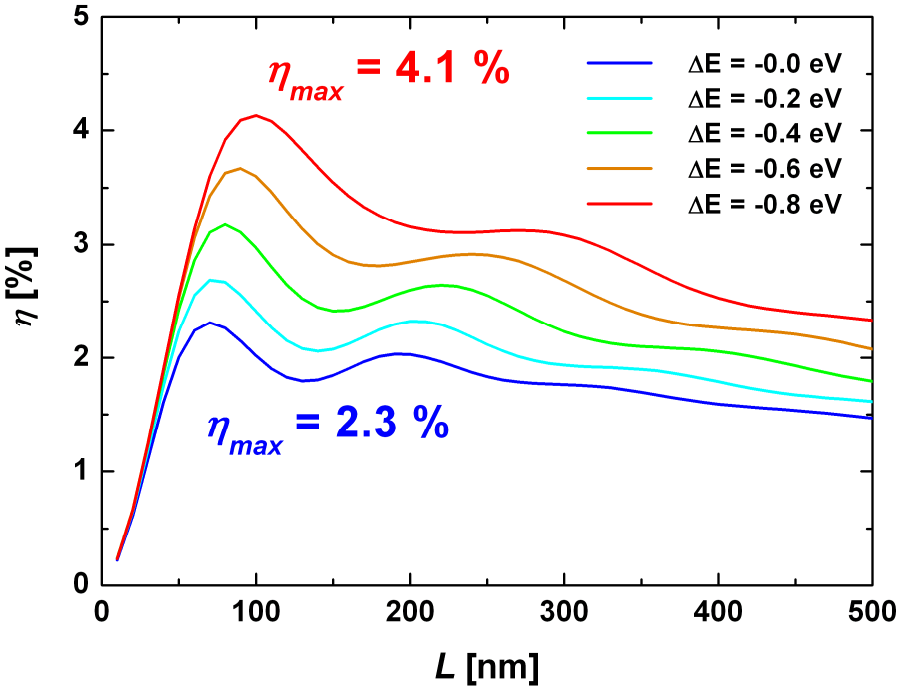

Figure 4.3: Efficiency η as a function of active layer thickness for a red-shift ΔE from 0 to 0.8 eV using μ_h = 2 x 10^{-8} m^2/Vs and μ_e = 2 x 10^{-7} m^2/Vs.

For MDMO-PPV (ΔE = 0) it was reported that the lowering of the efficiency with increasing thickness resulted from an increased recombination since the carriers have to travel a longer distance and an increase of the buildup of space-charges because the transport is not completely balanced.[25] Furthermore, with increasing active layer thickness also the electric fields are reduced that lower the dissociation efficiency. However, for ΔE = 0.8 eV the decrease of efficiency for thick devices is much stronger as compared to MDMO-PPV (ΔE = 0). Both loss processes have a negative effect on the fill factor (*FF*) of the solar cell. The question now is whether the strong efficiency decrease for low band gap cells is due to a recombination increase because of the increased carrier densities, or due to an enhanced buildup of space-charges.

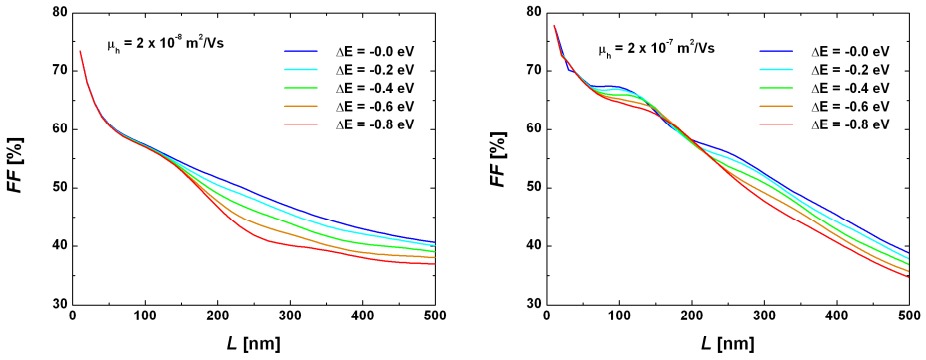

Figure 4.4a & b: Fill factor *FF* as a function of active layer thickness for red-shift ΔE from 0 to 0.8 eV in steps of 0.2 eV and hole mobility μ_h of 2 x 10^{-8} m^2/Vs (a) and 2 x 10^{-7} m^2/Vs (b).

4.4 Role of balanced transport

A way to evaluate the role of the various processes is to study the effect of an increase of the hole mobility μ_h to 2 x 10^{-7} m^2/Vs, such that the transport is balanced. In this way the effect of space-charge formation will be eliminated. Figure 4.4a shows the fill factor *FF* as a function of *L* for ΔE from 0 to 0.8 eV in steps of 0.2 eV and μ_e and μ_h of 2 x 10^{-7} m^2/Vs and 2 x 10^{-8} m^2/Vs respectively. As expected the *FF* decreases with increasing *L*, but for active layers thicker than 150 nm the curves for different band gap lowering ΔE start to diverge from each other. As a comparison the decrease of *FF* with increasing *L* is shown in figure 4.4b in case of balanced transport. In this case the curves start diverging from 50 nm onwards and show signs of oscillatory features. However, for all thickness the *FF* is substantially higher as compared to the unbalanced transport case. For example, around the second maximum (~250 nm) the *FF* in case of unbalanced transport is just below 40 %, whereas for balanced transport it is still slightly above 50 %. It should be noted that the imbalance in transport considered here is only one order of magnitude, which is typical for many polymer:fullerene cells. For a larger imbalance the *FF* drops even

more at these thicknesses. In order to evaluate the effect of charge balance we compare in figure 4.5 the efficiency η in case of balanced and unbalanced transport.

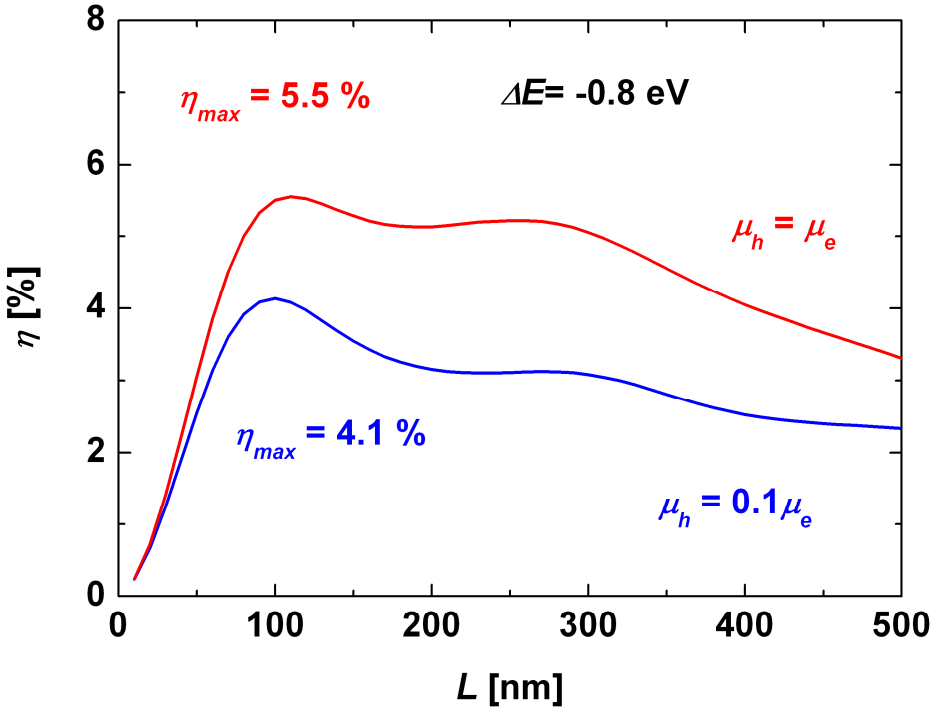

Figure 4.5: Efficiency η as a function of active layer thickness for a red-shift ΔE of 0.8 eV using μ_h of 2 x 10^{-8} m^2/Vs and μ_h = 2 x 10^{-7} m^2/Vs, respectively. The electron mobility μ_e amounts to 2 x 10^{-7} m^2/Vs.

The balancing of the charge transport in this low band gap cell (E_{gap} = 1.6 eV) leads to a strong increase of the efficiency, from 4.1 to 5.5 %. Furthermore, due to the balanced transport the absorption increase for low band gap cells is now also exploited in thicker cells (250 nm). The difference between the two interference maxima at 110 nm and 270 nm has almost disappeared. This result stresses the importance of balanced transport in low band gap polymer:fullerene solar cell. It should be noted that the recently reported values exceeding 7 % make us of the fullerene [70]PCBM that complements the absorption of the low band gap polymer and therefore broadens the total absorption spectrum of the polymer:fullerene cell. With [60]PCBM, as used in our modeling, efficiencies of around 5 % have been

reported, in agreement with our results on low band gap cells with balanced charge transport.

4.5 Conclusions

In conclusion, the effect of band gap lowering of the polymer absorber in polymer:fullerene bulk heterojunction solar cells is modeled. For devices thinner than 50 nm a lower band gap does not lead to an increased exciton generation. For 100 nm devices a shift of 0.8 eV from 2.4 eV to 1.6 eV leads to an efficiency increase of only 2.3 % to 4.1 %. Due to space-charge formation a mobility difference of only one order of magnitude strongly limits the performance of low band gap devices (1.6 eV) thicker than 200 nm. As a result balancing of the charge transport is more crucial for low band gap solar cells: The increased absorption leads to higher carrier densities and therefore also to an enhanced space-charge buildup.

References

[1] S. E. Shaheen, C. J. Brabec, N. S. Sariciftci, F. Padinger, T. Fromherz, and J. C. Hummelen, Appl. Phys. Lett. **78**, 841 (2001).

[2] F. Padinger, R. S. Rittberger, and N. S. Sariciftci, Adv. Funct. Mater. **13**, 85 (2003).

[3] J. Peet, J. Y. Kim, N. E. Coates, W. L. Ma, D. Moses, A. J. Heeger, and G. C. Bazan, Nat. Mater. **6**, 497 (2007).

[4] D. Mühlbacher, M. Scharber, M. Morana, Z. Zhu, D. Waller,R. Gaudiana, and C. Brabec, Adv. Mater. **18**, 2884 (2006).

[5] M. A. Green, K. Emery, Y. Hishikawa, and W. Warta, Prog. Photovoltaics **19**, 565 (2011).

[6] G. Li, V. Shrotriya, J. Huang, Y. Yao, T. Moriarty, K. Emery, and Y. Yang, Nat. Mater. **4**, 864 (2005).

[7] W.Ma, C. Yang, X. Gong, K. Lee, A. J. Heeger, Adv. Funct. Mater. **15**, 1617 (2005).

[8] V. D. Mihailetchi, H. Xie, B. de Boer, L. J. A. Koster, and P. W. M. Blom, Adv. Funct. Mater. **16**, 699 (2006).

[9] A. Dhanabalan, J. K. J. van Duren, P. A. van Hal, J. L. J. van Dongen, and R. A. J. Janssen, Adv. Funct. Mater. **11**, 255 (2005).

[10] X. Wang, E. Perzon, J. L. Delgado, P. de la Cruz, F. Zhang, F. Langa, M. R. Andersson, and O. Inganäs, Appl. Phys. Lett. **85**, 5081 (2004).

[11] F. Zhang, W. Mammo, L. M. Andersson, S. Admassie, M. R. Andersson, and O. Inganäs, Adv. Mater. **18**, 2169 (2006).

[12] M. M. Wienk, M. P. Struijk, and R. A. J. Janssen, Chem. Phys. Lett. **422**, 488 (2006).

[13] K. Colladet, S. Fourier, T. J. Cleij, L. Lutsen, J. Gelan, D. Vanderzande, L. H. Nguyen, H. Neugebauer, N. S. Sariciftci, A. Aguirre, G. Janssen, and E. Goovaerts, Macromolecules **40**, 65(2007).

[14] E. Perzon, F. Zhang, M. Andersson, W. Mammo, O. Inganäs, and M. R. Andersson, Adv. Mater. **19**, 3308 (2007).

[15] M. M. Wienk, M. Turbiez, J. Gilot, and R. A. J. Janssen, Adv. Mater. **20**, 2556 (2008).

[16] J. Hou, H.-Y. Chen, S. Zhang, G. Li, and Y. Yang, J. Am. Chem. Soc. **130**, 16144 (2008).

[17] S. Beaupre, P. L. T. Boudreault, and M. Leclerc, Adv. Mater. **22**, E6 (2010).

[18] L. J. A. Koster, V. D. Mihailetchi, and P. W. M. Blom, Appl. Phys. Lett. **88**, 093511 (2006).

[19] V. D. Mihailetchi, J. K. J. van Duren, P. W. M. Blom, J. C. Hummelen, R. A. J. Janssen, J. M. Kroon, M. T. Rispens, W. J. H. Verhees, and M. M. Wienk, Adv. Funct. Mater. **13**, 43 (2003).

[20] C. Melzer, E. Koop, V. D. Mihailetchi, and P. W. M. Blom, Adv. Funct. Mater. **14**, 865 (2004).

[21] L. A. A. Pettersson, S. Ghosh, and O. Inganäs, Organic Electronics **3**, 143–148 (2002).

[22] L. J. A. Koster, E. C. P. Smits, V. D. Mihailetchi, and P. W. M. Blom, Phys. Rev. B **72**, 085205 (2005).

[23] H. Hoppe, N. S. Sariciftci, and D. Meissner, Mol. Cryst. Liq. Cryst. Sci. Technol. Sect. A **385**, 113 (2002).

[24] D. R. Lide, *Handbook of Chemistry and Physics*, (CRC, Boca Raton 1994).

[25] M. Lenes, L. J. A. Koster, V. D. Mihailetchi, and P. W. M. Blom, Appl. Phys. Lett. **88**, 243502 (2006).

Chapter 5

Impact of unbalanced charge transport on the efficiency of normal and inverted solar cells

Summary

In a normal solar cell most charge carriers are generated close to the anode, such that electrons have to travel a longer distance as compared to the holes. In an inverted solar cell holes have to travel a longer distance. We use a combined optical and electronic model to simulate the effect of unbalanced transport on the efficiency of normal and inverted single- and tandem solar cells. When the electrons are ten times more mobile than the holes the efficiency for a single cell with a thickness of 250 nm drops from 7.5 to 4.5 % when changing from a normal to an inverted structure. For opposite mobility ratio the inverted structure clearly outperforms the normal structure.

5.1 Introduction

The common device structure for polymer based organic solar cells utilizes indium tin oxide (ITO) covered by poly(3,4-ethylenedioxythiophene) [PEDOT] doped with poly(4-styrenesulfonate) [PSS] as a transparent anode, followed by a photoactive polymer:fullerene blend and finally a suitable reflective cathode on top of it. A drawback of this normal device structure is that the ITO\PEDOT:PSS interface is unstable and diminishes organic solar cell performance over time.[1,2] One way of overcoming this drawback is to invert the structure of the device, so that an electrically conductive and transparent cathode is placed on the ITO and on top of the active material a suitable reflective anode, which has been successfully implemented in recent years.[3-11] A promising approach is the use of precursor zinc oxide to produce a layer of zinc oxide [ZnO] on the ITO layer that acts as a transparent cathode.[2] As reflecting anode a transparent layer of molybdenum trioxide [MoO_3] covered with aluminum [Al] has been used. When comparing the performance of normal and inverted solar cells it is expected that the amount of absorbed photons in both cases will be very similar. For both device structures the incoming light is reflected at the reflective end electrode, leading to a pattern of self-interfering light in the device and for sufficiently thin active layers (< 200 nm) this results in the majority of photons being absorbed near the transparent electrode, generating most of the charge carriers in that region.[12-15] However, when the charge transport in the solar cell is unbalanced the slowest charge carriers either will have to travel to the transparent electrode or to the reflective electrode, depending on the device geometry. In the former case, the average travel distance and time are relatively short, diminishing space-charge buildup and recombination losses. In the latter case, the average travel distance and time are relatively long, thus enhancing space charge buildup and related losses, and thereby decreasing device performance.[13,16] In this study we use combined optical and electrical modeling to simulate normal and inverted single and tandem solar cell devices with unbalanced transport. We

investigate what influence various ratios between electron and hole mobilities have on the overall performance of devices with normal and inverted geometries.

5.2 Definition of device stack and simulation parameters

As a first step we simulate single solar cells using a recently developed combined optical and electrical model.[12-15,17] A typical device stack is simulated and consists of a silica substrate of 0.75 mm thickness with on top of it a 130 nm thick layer of indium tin oxide (ITO). In the case of a normal device structure the ITO layer is covered with a 40 nm thick layer of poly(3,4ethylenedioxythiophene)/ poly(styrenesulfonic acid) (PEDOT:PSS) as transparent anode, a layer of the polymer:fullerene bulk heterojunction blend as active layer with varying thickness, and 1 nm of lithium fluoride (LiF) topped with 100 nm of aluminium (Al) as reflective cathode. In the case of an inverted device structure, on top of the ITO layer a 20 nm thick layer of zinc oxide (ZnO) as transparent cathode is used, then the polymer:fullerene bulk heterojunction blend as active layer, a 10 nm thick layer of molybdenum trioxide (MoO_3) as transparent anode covered with a 100 nm thick layer of Al as reflective electric contact. Necessary for simulating the optical performance of these devices are the optical properties of the materials. Those of MoO_3 and Al are taken from literature,[18,19] those of silica, ITO, PEDOT:PSS, ZnO and LiF were determined with a Woollam variable-angle spectroscopic ellipsometer (VASE) by variable angle ellipsometry. The optical properties of the polymer:fullerene blend have been previously used,[20] with the blend consisting of a polymer:fullerene mixture in a 2 to 1 volumetric ratio for a polymer band gap of 1.7 eV.[20] In the simulations the thickness of the active layer is varied between 10 and 250 nm in steps of 10 nm. For the electrical part of the modeling we take the energy levels of the lowest unoccupied molecular orbital (LUMO) and the highest occupied molecular orbital (HOMO) of the fullerene to be 3.8 and 6.1 eV and of the polymer to be 3.5 and 5.2 eV, respectively. With a minimal loss of 0.6 eV with respect to the optical band gap[21] an open circuit voltage V_{oc} of typically 1 eV is used. Further electronic

parameters of the active layer used in the electronic device model are temperature T = 295 K, relative dielectric constant ε_r = 3.4, charge pair separation a = 1.8 nm and bound e-h pair decay rate $k_f = 2\times10^4$ s^{-1}, being similar to slowly dried P3HT:PCBM cell parameters.[22] The electron and hole mobilities $\mu_{e,h}$ are varied between 10^{-10}, 10^{-9}, 10^{-8} and 10^{-7} m^2/Vs, with the latter being an optimum value.[22] The ratio between μ_e and μ_h, μ_e/μ_h, is varied between 0.001 and 1000 in scale steps of 10, with the highest mobility being fixed at the optimum value of 10^{-7} m^2/Vs. In this way the effect of unbalanced transport for the normal and inverted device configuration can be visualized as a function of the μ_e/μ_h ratio.

5.3 Results

A. Single cells

First we verify that the optical absorption for both device structures is identical. In Figure 5.1 the optical absorption profile of a device with a 100 nm thick active layer are shown for both device structures. As can be seen from the absorption profiles, the expected maximum of absorption due to interference is observed as well as the typical quadratic like increase in absorption near the reflective electrode, both due to the self-interference of the incoming light. As expected, the majority of charge carriers is generated near the active layer's side of light influx, which is also the case for other L and is independent of device structure. In more detail, the inverted cell's absorption profile is shifted about 10 nm toward the reflective electrode with regard to the normal cell's absorption profile due to the 9 nm difference in thickness between the transparent LiF and MoO_3 layers. Furthermore, it has a slightly lower absorption maximum than the normal cell's absorption profile. In order to determine which device structure leads to a higher total absorption of light inside the active layer we integrate the absorption profile over the active layer thickness.

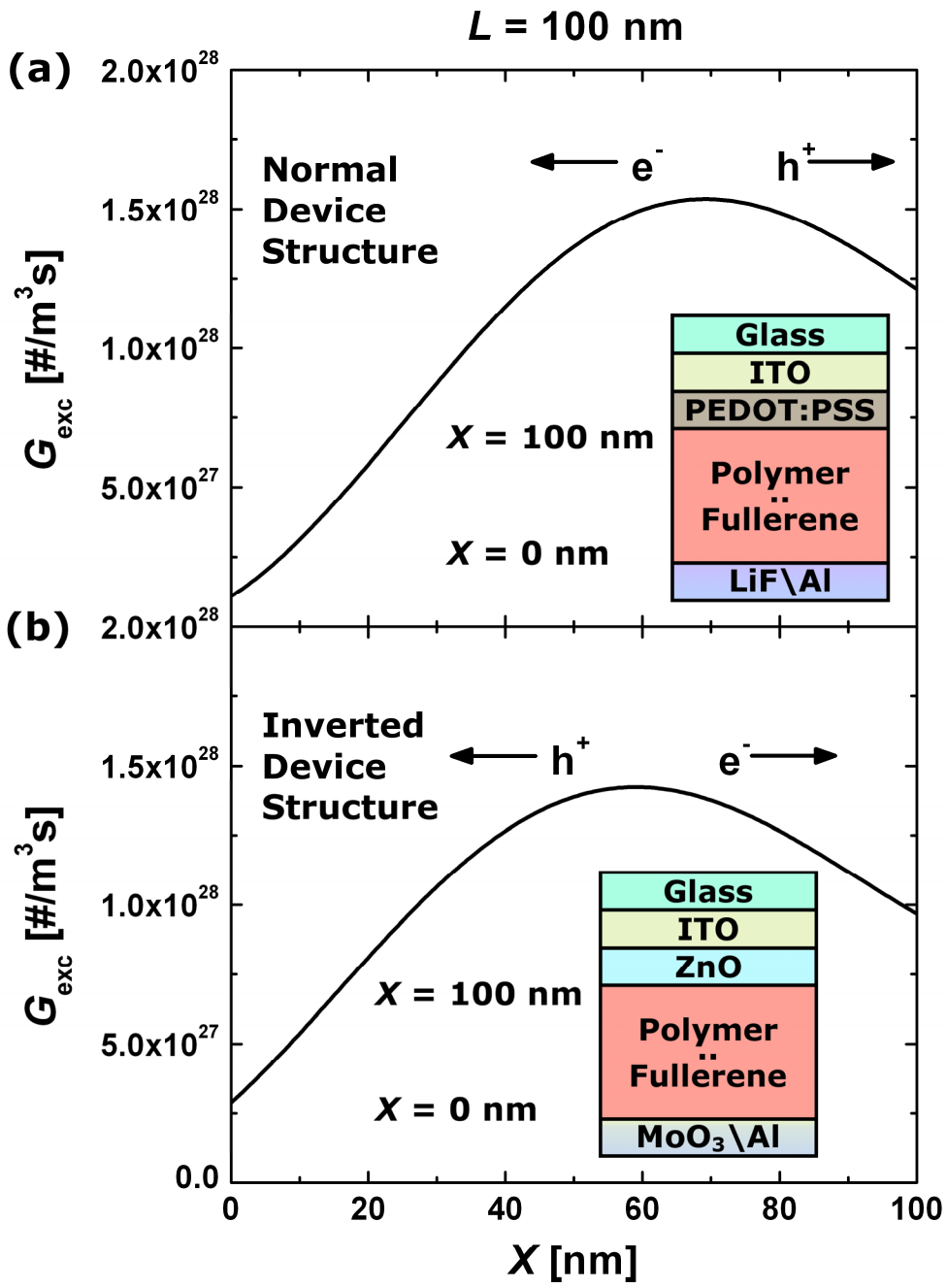

Figure 5.1a+b: Optical absorption rate G_{exc} showing the absorption profile of two 100 nm thick active layers in normal (a) and inverted (b) single device structures. *X* denotes the distance from the boundary between the active layer and the reflective electrode. Note the small shift of the absorption profile for the two different device structures.

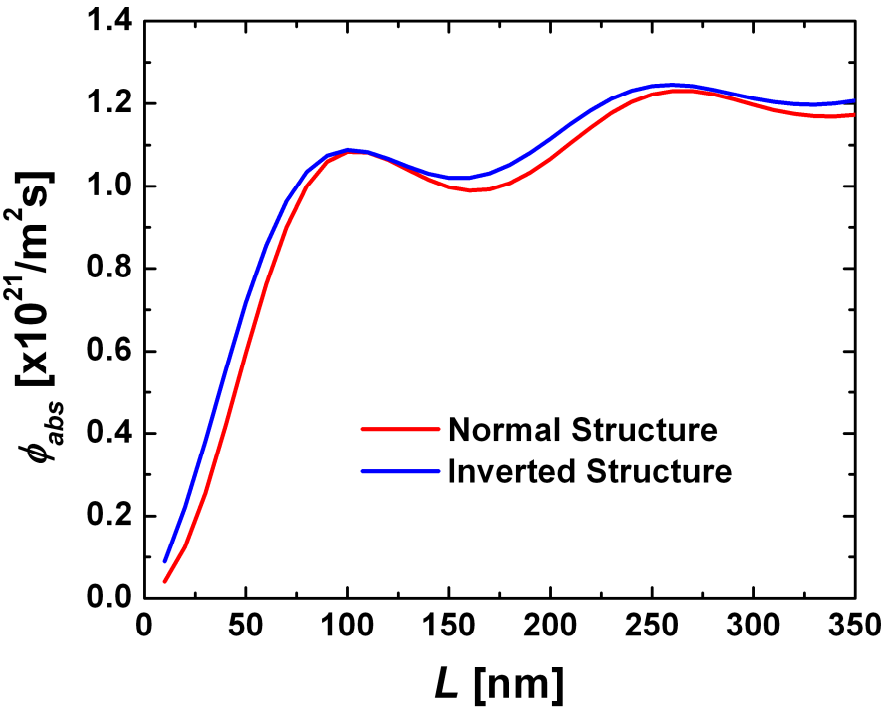

Figure 5.2: Total optical absorption in the active layer Φ_{abs} as a function of active layer thickness L for normal and inverted single device structures. Note that Φ_{abs} is slight shifted to the left for the inverted device structure as compared to the normal one.

The result of this calculation for different L is displayed in Figure 5.2, where the total absorption of photon flux is shown as a function of L for the normal and inverted device structures as a function of active layer thickness. It appears that the total absorbed flux of the normal and inverted device are very similar, the only difference is a small shift in thickness due to the abovementioned difference in the electrode stack. Both device structures have the optimum absorption around 100 and 250 nm active layer thickness, respectively.

As a next step we compare the electrical performance of single solar cells with normal or inverted device structures as a function of μ_e/μ_h for active layer thicknesses of 100 (Figure 5.3a) and 250 nm (Figure 5.3b), respectively.

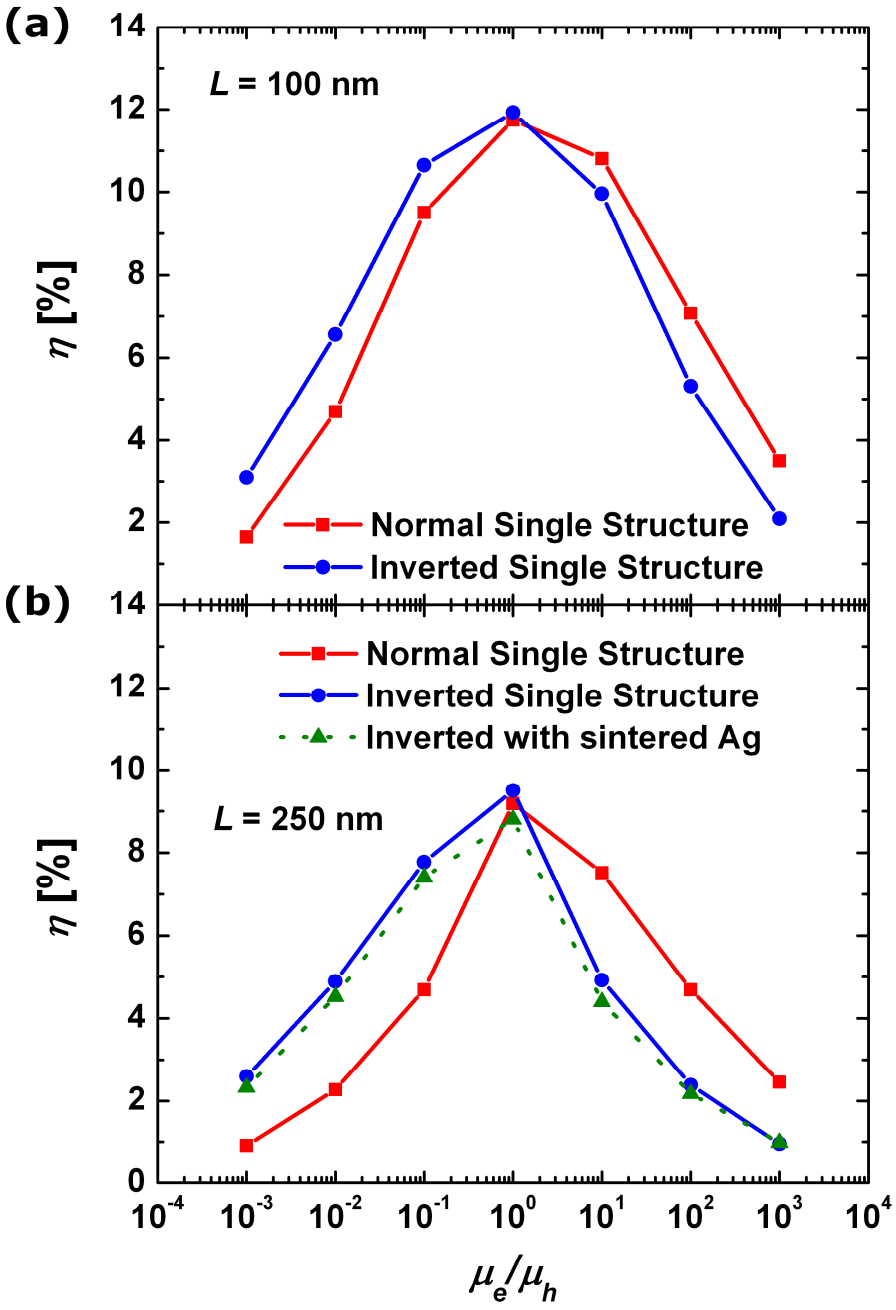

Figure 5.3: Power conversion efficiency η for different electron and hole mobility ratios μ_e/μ_h of normal and inverted single device structures for an active layer thickness L of 100 nm (a) and 250 nm (b). In (b) there is an additional set of simulated data for inverted devices with a less reflective Ag electrode. Note that the performance difference between normal and inverted devices for unbalanced charge transport is significantly bigger for 250 nm thick devices than 100 nm thick ones.

As expected for unbalanced charge transport, the overall performance of the devices becomes worse for increasing or decreasing μ_e/μ_h, clearly showing the detrimental effects of increased space charge buildup and recombination on the device performance. From Figure 5.3a it is observed that for a 100 nm thick solar cell the device performance already drops significantly from the calculated 12 % efficiency for a fully optimized inverted device to almost 10% for devices with the slowest charge carriers having a 10 times lower mobility than the fastest ones. Furthermore when electrons are the slowest charge carriers, the inverted device structure has the best performance, which is usually the case for polymer:polymer devices. When holes are the slowest charge carriers, the normal device structure has the best performance, which is the case for most polymer:fullerene devices. In that case a change from normal to inverted geometry would lead to an efficiency loss from 12 to 10 %. However, for large-area roll-to-roll processed solar cell devices with a 250 nm active layer are far more attractive due to an improved homogeneity of the layer thickness and improved robustness for electrical shorts, leading to a higher production yield. However, for this thicker layer the distances that the slowest carriers have to travel become larger, making the effects of unbalanced charge transport even more pronounced. As shown in Figure 5.3b when the holes are ten times slower than the electrons the efficiency drops from 7.5 to 4.5 %, when changing from a normal to an inverted device. In case that the holes are ten times faster than the electrons the inverted solar cell has a calculated efficiency of 8 % compared to an efficiency of only 5 % for the normal cell. These calculations clearly demonstrate that when making a choice for a normal or inverted geometry, either for stability or production reasons, the balance of the charge transport is a vital parameter that needs to be considered. Additionally, commercial roll-to-roll processed solar cells have nanoparticle metal ink films deposited onto the active layer, which is sintered to yield a porous yet conductive metal electrode. As this metal layer is assumed to be less reflective than vacuum deposited one, this will change the interference pattern of the light inside the active layer, which could intensify the effects of the imbalanced charge transport. We investigated the influence of a less reflective metal electrode on inverted devices by making use of the optical properties of deposited silver (Ag) ink films after sintering for 18 minutes as reported by Pan et *al.*[23] for the modeling of a

less reflective Ag anode on top of the MoO_3 interlayer. As can be seen in Figure 5.3b, the Ag electrode diminishes the performance of the inverted device by a relatively small amount. This demonstrates that the decreased reflectivity of metal electrodes in commercial roll-to-roll organic photovoltaics only marginally decreases their performance.

B. Tandem cells

To achieve higher efficiencies a lot of attention has recently been paid to tandem solar cells.[24] Tandem device structures are based upon the single device structures, but with three extra layers in case of two sub-cells that are connected in series. Also here a choice between a normal or inverted device structure can be made. The normal tandem structure is built up as follows: A 0.75 mm silica substrate with on top of it a 130 nm thick layer of ITO as transparent electric contact, a 40 nm thick layer of PEDOT:PSS as transparent anode, a variably thick layer of polymer:fullerene bulk heterojunction blend as back active layer, a 20 nm thick layer of ZnO as transparent cathode, a 40 nm thick layer of neutralized PEDOT:PSS[5,25] as transparent anode, a variably thick layer of polymer:fullerene bulk heterojunction blend as back active layer and a 1 nm thick layer of LiF and a 100 nm thick layer of Al as reflective cathode. The inverted tandem is structured as follows: A 0.75 mm silica substrate with on top of it a 130 nm thick layer of ITO as transparent electric contact, a 20 nm thick layer of ZnO as transparent cathode, a variably thick layer of polymer:fullerene bulk heterojunction blend as front active layer, a 40 nm thick layer of PEDOT:PSS as transparent anode, a 20 nm thick layer of ZnO as transparent cathode, a variably thick layer of polymer:fullerene bulk heterojunction blend as back active layer, a 10 nm thick layer of MoO_3 as transparent anode, and a 100 nm thick layer of Al as reflective electric contact. The front and back active layers, however, have now different optical and electrical characteristics, as the optimized polymer band gaps for both layers in a tandem device differ from that in a single celled device.[20] An optimum performance for tandem devices is obtained for polymer band gaps of 1.9 eV and 1.5 eV for the front and back device, respectively.[20] The energy levels of the fullerene are the same for both active layers, being 3.8 eV for the LUMO and 6.1 eV for the HOMO. The

LUMO and HOMO energy levels of the front layer polymer are 3.5 and 5.4 eV respectively, those of the back layer polymer are 3.5 eV and 5.0 eV respectively. This will result in a V_{oc} of 1.3 V for the front device and 0.9 V for the back device, adding up to a tandem V_{oc} of slightly over 2 V. In order to study the role of unbalanced transport both μ_e and μ_h are taken to be the same for both active layers.

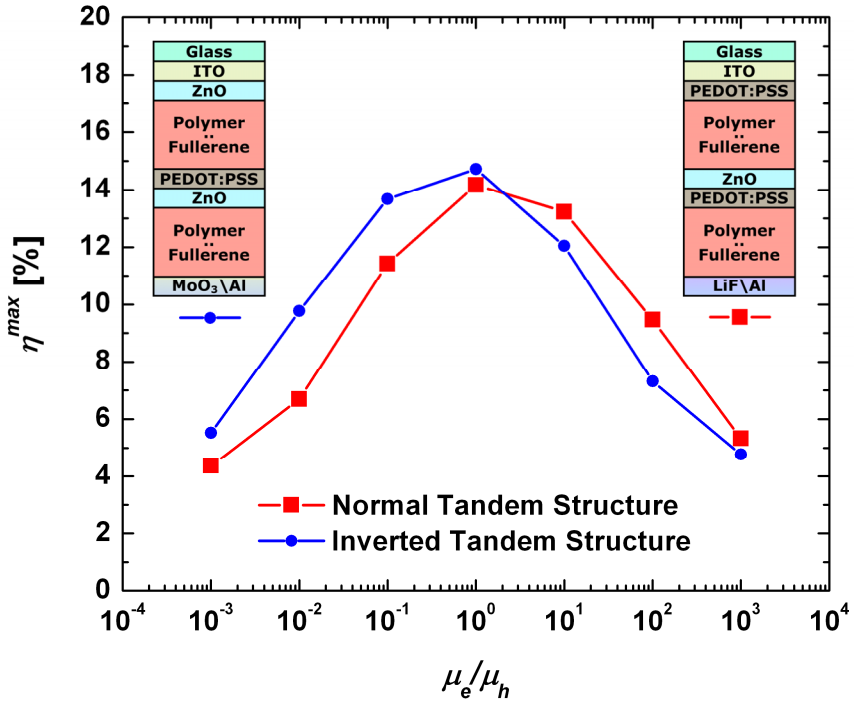

Figure 5.4: Optimized power conversion efficiency η^{max} for different electron and hole mobility ratios μ_e/μ_h of normal and inverted tandem device structures. Note that for μ_e/μ_h = 0.001 and 1000 the difference in η^{max} for normal and inverted device structures is significantly smaller than for single devices.

Figure 5.4 shows the optimized *PCE* of tandem devices with normal or inverted device structures as a function of μ_e/μ_h. In this calculation for every mobility ratio μ_e/μ_h the layer thicknesses of the front and back device have been optimized for both device geometries. Again the detrimental influence of μ_e/μ_h being unequal to unity on the space charge buildup and the device performance can be observed. The

overall trend of the performance is similar to that of the single device with a layer thickness of 100 nm, yet a few differences are present. First of all, each tandem device performs better than its single device counterpart sharing device structure and mobility ratio. Furthermore, the devices with the worst performing device structure having a μ_e/μ_h of 0.001 or 1000 are closer to the performance of their better performing counterparts with the other device structure. For these mobility ratios the optimum active layers for the front and back devices are very thin [< 50 nm], which means that space-charge buildup related losses have far less impact. Here, it is mainly the diminished absorption in the thin layers that limits the attainable device performance. Again for electrons being the slowest charge carriers the inverted tandem structure yields the best performances, which is best suited for polymer:polymer tandem devices. For holes being the slowest charge carriers the normal tandem structure performs better, as is the case for most polymer:fullerene tandem solar cells with unbalanced charge transport. In case of balanced transport both device geometries perform equally well.

5.4 Conclusions

In conclusion, the influence of unbalanced charge transport on the performance of normal and inverted solar cells has been studied by simulations using a combined optical and electrical model. For single cells with a favorable thickness of 250 nm the normal device structure clearly outperforms the inverted structure for devices with slower hole transport, like most polymer:fullerene devices. Vice versa, the inverted device structure is optimal for devices with slower electron transport, like polymer:polymer devices. For balanced transport the performance is equal such that other factors as lifetime and production yield decide the optimal device structure. It has been shown that this holds as well for tandem devices, assuming that the same mobility ratio is used for both sub-cells.

References

[1] M. P. de Jong, L. J. van IJzendoorn, and M. J. A. de Voigt, Appl. Phys. Lett. **77**, 2255 (2000).

[2] K. W. Wong, H. L. Yip, Y. Luo, K. Y. Wong, W. M. Lau, K. H. Low, H. F. Chow, Z. Q. Gao, W. L. Yeung, and C. C. Chang, Appl. Phys. Lett. **80**, 2788 (2002).

[3] J. Gilot, I. Barbu, M. M. Wienk, and R. A. J. Janssen, Appl. Phys. Lett. **91**, 113520 (2007).

[4] P. de Bruin, D. J. D. Moet, and P. W. M. Blom, Organic Electronics **11**, 1419 (2010).

[5] T. J. K. Brenner, I. Hwang, N. C. Greenham, and C. R. McNeill, J. Appl. Phys. **107**, 114501 (2010).

[6] X. W. Sun, D. W. Zhao, L. Khe, A. K. K. Kyaw, G. Q. Lo, and D. L. Kwong, Appl. Phys. Lett. **97**, 053303 (2010).

[7] C.-H. Chou, W. L. Kwan, Z. Hong, L.-M. Chen, and Y. Yang, Adv. Mater. **23**, 1282 (2011).

[8] S. K. Hau, H.-L. Yip, K.-S. Chen, J. Zou, and A. K.-Y. Jen, Appl. Phys. Lett. **97**, 253307 (2010).

[9] D. W. Zhao, L. Ke, S. T. Tan, A. K. K. Kyaw, H. V. Demir, X. W. Sun, D. L. Carroll, G. Q. Lo, and D. L. Kwong, Sol. Energy Mater. **95**, 921, (2011).

[10] J.-C. Wang, W.-T. Weng, M.-Y. Tsai, M.-K. Lee, S.-F. Horng, T.-P. Perng, C.-C. Kei, C.-C. Yu, and H.-F. Meng, J. Mater. Chem. **20**, 862 (2010).

[11] H.-J. Park, K.-H. Lee, B. Humar, K.-S. Shin, S.-W. Jeong, and S.-W. Kim, J. Nanoelectron. Ooptoelectron. **5**, 1 (2010).

[12] A. A. Pettersson, L. S. Roman, and O. Inganäs, J. Appl. Phys. **86**, 487 (1999).

[13] H. Hoppe, N. Arnold, N. S. Sariciftci, and D. Meissner, Sol. Energy Mater. **80**, 105 (2003).

[14] N.-K. Persson, H. Arwin, and O. Inganäs, J. Appl. Phys. **97**, 034503 (2005).

[15] J. D. Kotlarski, P. W. M. Blom, L. J. A. Koster, M. Lenes, and L. H. Slooff, J. Appl. Phys. **103**, 084502 (2008).

[16] V. D. Mihailetchi, L. J. A. Koster, J. C. Hummelen, and P. W. M. Blom, Phys. Rev. Lett. **94**, 126602 (2004).

[17] L. J. A. Koster, E. C. P. Smits, V. D. Mihailetchi, and P. W. M. Blom, Phys. Rev. B **72**, 085205, (2005).

[18] T. S. Sian, G. B. Reddy, Sol. Ener. Mater. & Sol. Cells **82**, 375 (2004).

[19] D. R. Lide, *Handbook of Chemistry and Physics* (CRC, Boca Raton, 1994).

[20] J. D. Kotlarski, and P. W. M. Blom, Appl. Phys. Lett. **98**, 053301 (2011).

[21] D. Veldman, C. S. J. Meskers, R. A. J. Janssen, Adv. Funct. Mater. **19**, 1939 (2009).

[22] V. D. Mihailetchi, H. Xie, B. de boer, L. M. Popescu, J. C. Hummelen, P. W. M. Blom, and L. J. A. Koster, Apll. Phys. Lett. **89**, 012107 (2006).

[23] H. Pan, S. H. Ko, and C. P. Grigoropolous, Appl. Phys. Lett. **93**, 234104 (2008).

[24] A. Hadipour, B. de Boer, J. Wildeman, F. B. Kooistra, J. C. Hummelen, M. G. R. Turbiez, M. M. Wienk, R. A. J. Janssen, and P. W. M. Blom, Adv. Funct. Mater.**, 16**, 1897 (2006).

[25] D. J. D. Moet, P. de Bruyn, and P. W. M. Blom, Appl. Phys. Lett. **96**, 153504 (2010).

Chapter 6

Ultimate performance of polymer:fullerene bulk heterojunction tandem solar cells

Summary

We present the model calculations to explore the potential of polymer:fullerene tandem solar cells. As an approach we use a combined optical and electrical device model, where the absorption profiles are used as starting point for the numerical current-voltage calculations. With this model a maximum power efficiency of 11.7 % for single cells has been achieved as a reference. For tandem structures with a ZnO/poly(3,4-ethylenedioxythiophene)/poly(styrenesulfonic acid) middle electrode an ultimate efficiency of 14.1 % has been calculated. In the optimum configuration the subcell with the narrowest band gap is placed closest to the incoming light. Consequently, tandem structures are expected to enhance the performance of optimized single cells by about 20 %.

6.1 Introduction

In the past years, theoretical studies have been undertaken to understand what the fundamental performance limits are for organic bulk heterojunction solar cells.[1,2] These studies predict a practical power conversion efficiency limit of about 10 % – 11 % for single cells. The efficiency calculations done by Koster *et al.*[1] employed an electrical model including field and temperature dependent dissociation of bound electron – hole pairs as well as space-charge formation in the case of unbalanced charge transport.[3] The model was based on the assumption that the optical profile can be taken as constant and that the photocurrent is directly dependent on the total amount of absorbed photon flux. In a later stage we extended this model to a combined optical and electrical model.[4] The combined optical and electrical calculations confirmed that the exact shape of the absorption profile in the solar cells is not very critical as long as the active layer thickness (ALT) does not exceed 250 nm.[4] As a result the estimation of a maximum efficiency of 11 % for a single cell, done with a constant profile, is expected to be approximately correct. For organic tandem solar cells an estimation of the maximum efficiency was presented by Dennler *et al.*[5] Their calculations are mainly based on optical considerations. For the electrical part a number of assumptions were used; for example, the fill factor (FF) of the subcells was assumed to be 0.65, the external quantum efficiency was fixed at 65 %, the current of the tandem cell was taken equal to current of the subcell with the lowest current, and it was assumed that the FF of the tandem was identical to the FF of the subcells. An electrical device model for tandem solar cells was recently developed by Hadipour *et al.*[6] It was demonstrated how the $J - V$ characteristics of a tandem cell can be constructed from the characteristics of the two subcells. In case of an unequal current generation the middle electrode is charged, thereby enhancing the electric field and photocurrent of the current limiting cell. As a result the current of the tandem solar cell is higher than the current of the limiting cell. This effect was also demonstrated experimentally by Gilot *et al.*[7] In order to accurately estimate the ultimate efficiency of organic tandem solar cells a combined optical and electrical

approach is required. In this study, we extended the combined optical and electrical model from single cells to tandem cells. We demonstrate that a single organic solar cell has a maximum power conversion efficiency (η_{max}) of 11.7 %, whereas for a tandem cell a maximum efficiency η_{max} = 14.1 % is calculated. As a result with tandem cells an efficiency increase of about 20 % can be realized as compared to a fully optimized single cell.

6.2 Maximum efficiency of a single cell

As a first step toward the calculation of the maximum efficiency of a tandem cell we first reevaluate the efficiency calculations on single cells. We start with modeling of the optical properties of a typical single junction solar cell stack. As a substrate a 0.75 mm thick silica is taken with, on top of it, a 130 nm thick layer of indium tin oxide (ITO) as transparent front contact, a 40 nm thick layer of poly(3,4ethylenedioxythiophene)/poly(styrenesulfonic acid) (PEDOT:PSS) as transparent anode, a layer of a polymer:fullerene blend with variable thickness as active layer, and 1 nm of evaporated lithium fluoride (LiF) and 100 nm of evaporated aluminum (Al) as cathode. The optical properties of Al were taken from literature[8] and those of silica, ITO, PEDOT:PSS, and LiF were determined by variable angle ellipsometry using a Woollam variable-angle spectroscopic ellipsometer (VASE). The optical parameters of the polymer:fullerene blend are proposed to be an admixture of those of the polymer and those of the fullerene added in a 2:1 ratio, which is their volumetric ratio instead of their mass ratio, which is 1:1. The optical properties of the fullerene part are taken to be those of methanofullerene [6,6]-phenyl C_{61}-butyric acid methyl ester (PCBM) as reported by Hoppe *et al.*[9] Those of the polymer part are based on the properties of MDMO-PPV, as have been determined by variable angle ellipsometry using a Woollam VASE ellipsometer, but in the calculations the band gap B_{gap} is varied. The optical parameters of the polymer as a function of B_{gap}, together with those of PCBM, are shown in Figure 6.1. As can be seen in Figure 6.1, B_{gap} is varied between 1.4 and 2.2 eV in steps of 0.1 eV.

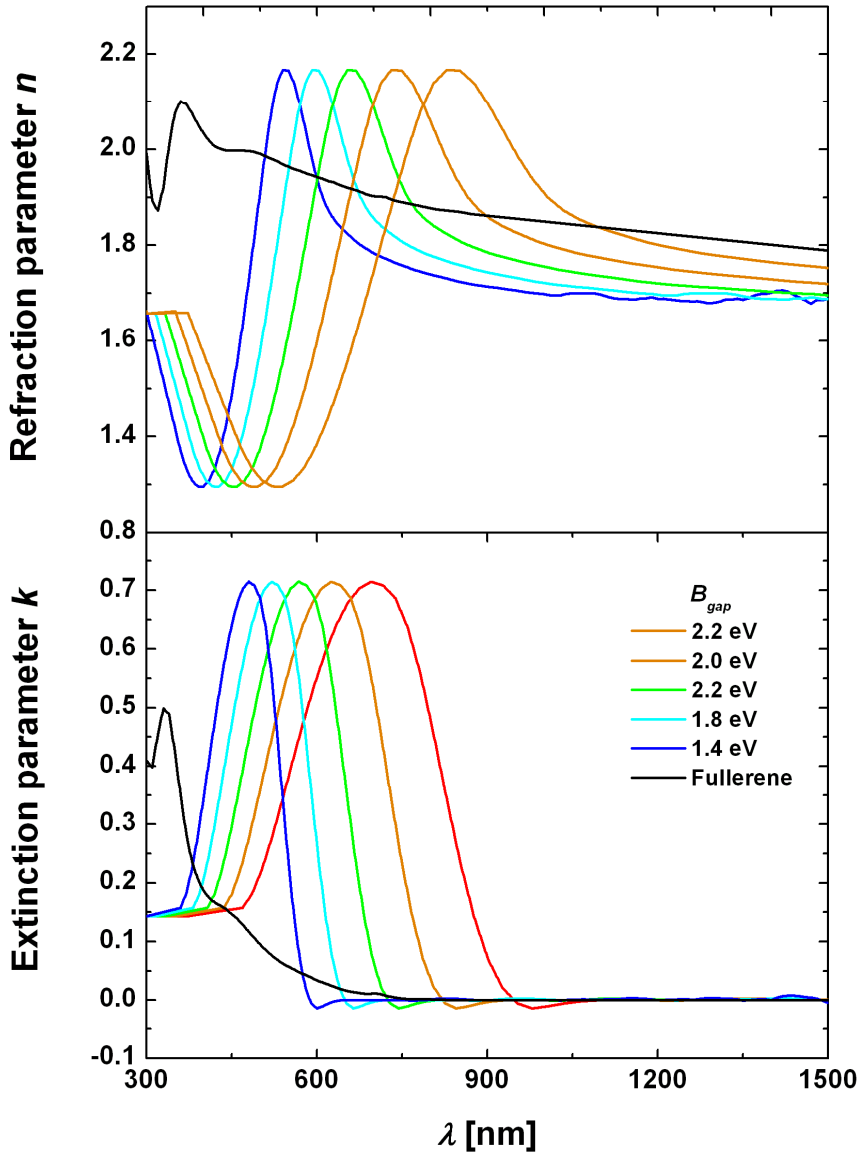

Figure 6.1: Complex refractive parameters of the polymer for five different B_{gap} and of the fullerene as a function of wavelength λ. Note that the polymer parameters are redshifted for B_{gap} lower than 2.2 eV.

The complex refractive parameters of the polymer with B_{gap} = 2.2 eV are those of MDMO-PPV, while those having a lower B_{gap} are redshifted by an amount of energy

equal to the 2.2 eV minus B_{gap}. We take the electronic energy levels of the lowest unoccupied molecular orbital (LUMO) and the highest occupied molecular orbital (HOMO) of the fullerene and polymer to be 3.8 and 6.1 eV (PCBM) and 3.5 and 4.9 – 5.7 eV (polymer) varied in steps of 0.1 eV, respectively. The difference of 0.3 eV between the polymer and fullerene LUMO levels is the assumed minimum necessary energy difference required for efficient electron transfer.[3] As a result of this reduction of 0.3 eV the energy gap between the LUMO of the fullerene and the HOMO of the polymer varies between 1.1 and 1.9 eV in steps of 0.1 eV in our calculations. With a typical loss of 0.4 eV from the energy gap to the open circuit voltage (V_{OC}) the resulting V_{OC} varies from 0.7 to 1.5 eV in steps of 0.1 eV. The electrical parameters of the active layers used in the electronic device model are temperature T = 295 K, relative dielectric constant ε_r = 3.4, electron and hole mobilities $\mu_{n,p} = 10^{-7}$ m^2/Vs, which is an optimum value,[10] charge pair separation a = 1.8 nm, and decay rate of the bound e – h pair $k_f = 2\times10^4$ s^{-1}, which are similar to the parameters obtained for slowly dried P3HT:PCBM cells.[11] An equal mobility for electrons and holes avoids efficiency losses due to too slow or unbalanced charge transport with resulting space-charge formation.

Using these parameters a single cell is simulated as a reference, with its ALT being varied between 10 and 250 nm with a step size of 10 nm and B_{gap} being varied between 1.4 and 2.2 eV with a step size of 0.1 eV. In Figure 6.2 the power conversion efficiency (η) is shown as a function of B_{gap} and ALT. Clearly visible is the maximum efficiency η_{max} = 11.7 % for B_{gap} = 1.7 eV and ALT = 100 nm, where V_{oc} = 1.00 V, the short-circuit current (J_{sc}) is 156.5 A/m^2, and the FF is 74.3 %. There is also a second efficiency maximum of 9.9 % for B_{gap} = 1.9 eV and ALT = 220 nm. The η_{max} is similar in magnitude to η_{max} found by Liang *et al.*,[12] where the optical absorption profile was taken as a constant. In the calculations presented here also the optical absorption profiles are taken into account, but since the relevant sample thicknesses do not exceed 250 nm the results are very similar. The two main factors that determine η_{max} are the absorbed photon flux and B_{gap}. With regard to B_{gap}, it is clear that narrower band gaps will increase the overlap with the solar spectrum, such that more photons are being absorbed and thus η increases. On the other hand, a smaller

B_{gap} also limits the V_{oc} of the cell. The resulting η_{max} is the best compromise, with the ALT such that the absorbance is in an interference maximum of the incoming photon flux.

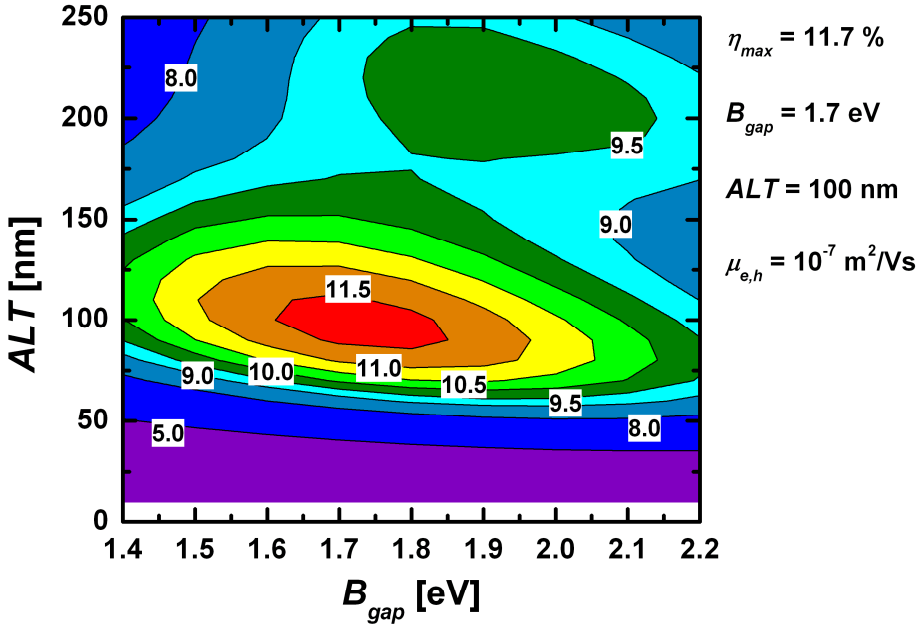

Figure 6.2: Power conversion efficiency η as a function of polymer band gap B_{gap} and ALT. Note that the sub-maximum has a higher B_{gap} because of the larger ALT.

6.3 Maximum efficiency of tandem cells

The tandem cell structure is similar to that of the single cell but has an additional middle electrode and a second active layer between the first active layer and the cathode. As middle electrode a 30 nm thick layer of zinc oxide (ZnO) is taken in combination with a 40 nm thick layer of neutralized PEDOT:PSS.[13,14] This layer serves as the transparent anode of the second active layer consisting also of a polymer:fullerene blend. The layer thickness of the two active layers is varied

between 10 and 250 nm in steps of 10 nm. The tandem cells are electrically connected in series. Hadipour *et al.*[6] developed a generalized methodology, which obtains the current-voltage characteristic of organic tandem solar cells by knowing the electrical performance of both subcells. Here, we use this methodology to calculate the performance of the tandem cells. The ALT and B_{gap} of each cell are varied individually like in the single cell scenario, resulting in 25×25×9×9 ≈ 50.000 different tandem cell variations. In Figure 6.3 the optical absorption profile is shown for an optimized tandem cell.

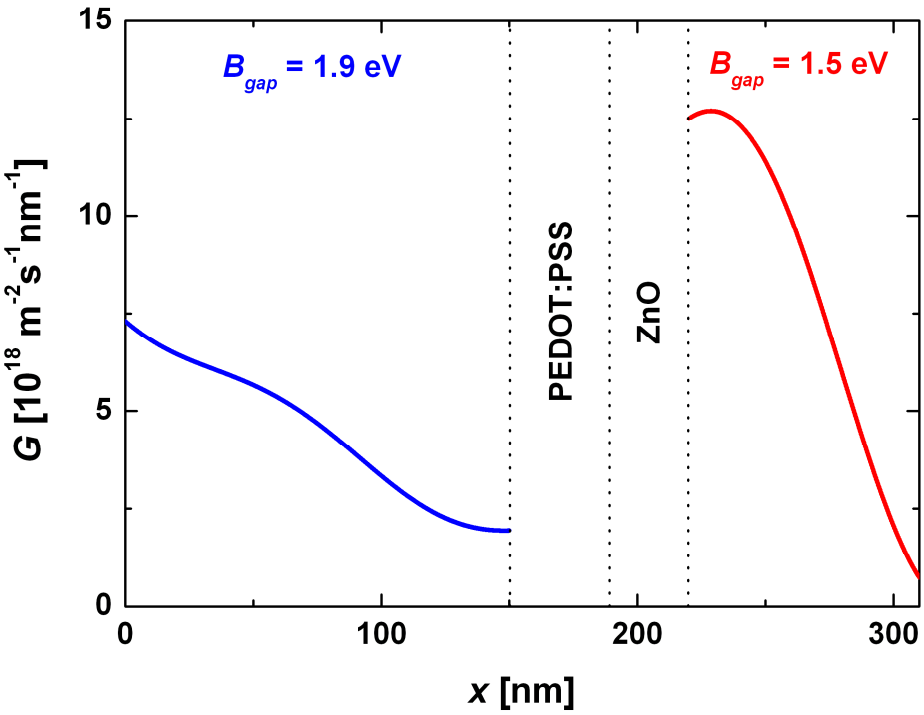

Figure 6.3: Calculated exciton generation rate profiles plotted vs the position *x* in an optimized tandem solar cell. Note that *G* is the rate of generated excitons per square meter per second per nanometer thickness of an active layer.

The front cell has a band gap B_{gap}^{front} and the back cell has a band gap B_{gap}^{back}, where the front cell is the subcell nearest to the glass substrate and the back cell is the subcell nearest to the Al cathode. The layer thicknesses of the front active layer [front layer

thickness (FLT)] and back active layer [back layer thickness (BLT)] amount to FLT = 150 nm and BLT = 90 nm, respectively. For these layer thicknesses the interference pattern is such that the absorption for both cells is maximized at these band gaps. Due to the four variables that determine the performance (B_{gap}^{front} , B_{gap}^{back} , FLT, and BLT) and that only two of them can be simultaneously displayed in a plot, we show η as a function of the front cell band gap B_{gap}^{front} and the back cell band gap B_{gap}^{back} in Figure 6.4.

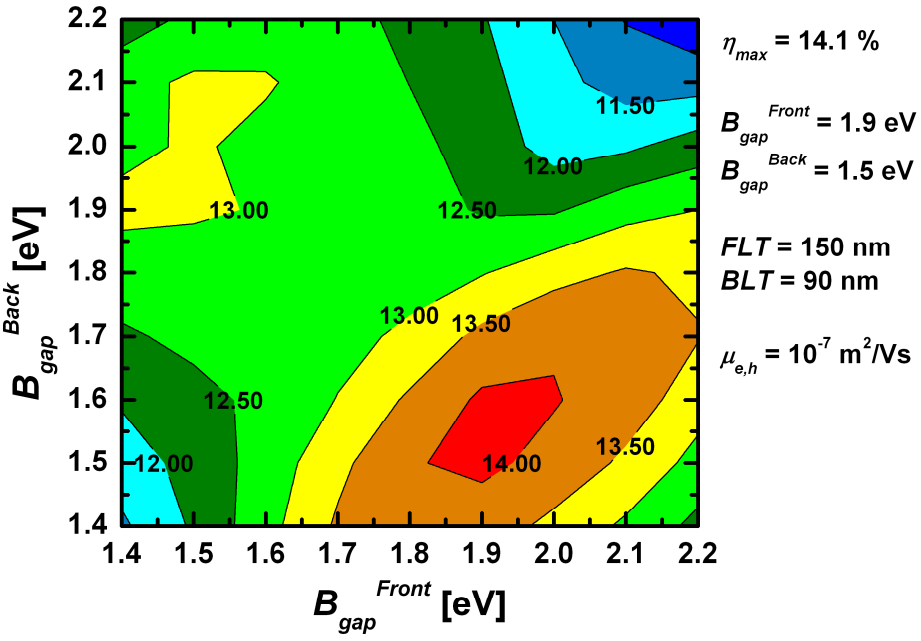

Figure 6.4: Power conversion efficiency η as a function of front layer polymer band gap B_{gap}^{front} and back layer polymer band gap B_{gap}^{back}. Note that 81 efficiencies in the plot are maximized with respect to FLT and BLT.

Note that each value of η for a pair of band gap values is the highest one for all FLT and BLT combinations considered. We obtain a maximum efficiency of the tandem cell of η_{max} = 14.1 % for B_{gap}^{front} = 1.9 eV, B_{gap}^{back} = 1.5 eV, FLT = 150 nm, and BLT =

90 nm. These numbers are comparable to the predictions made by Dennler *et al.*[5] and Ameri *et al.*,[15] with similar band gaps for the front and back subcells. A comparison with the single cell case (11.7 %) shows a maximum efficiency increase of 20 %, which is a significant improvement, but it is far less than a doubling of the efficiency. In Figure 6.5 the J – V characteristics of this best performing tandem cell configuration is shown.

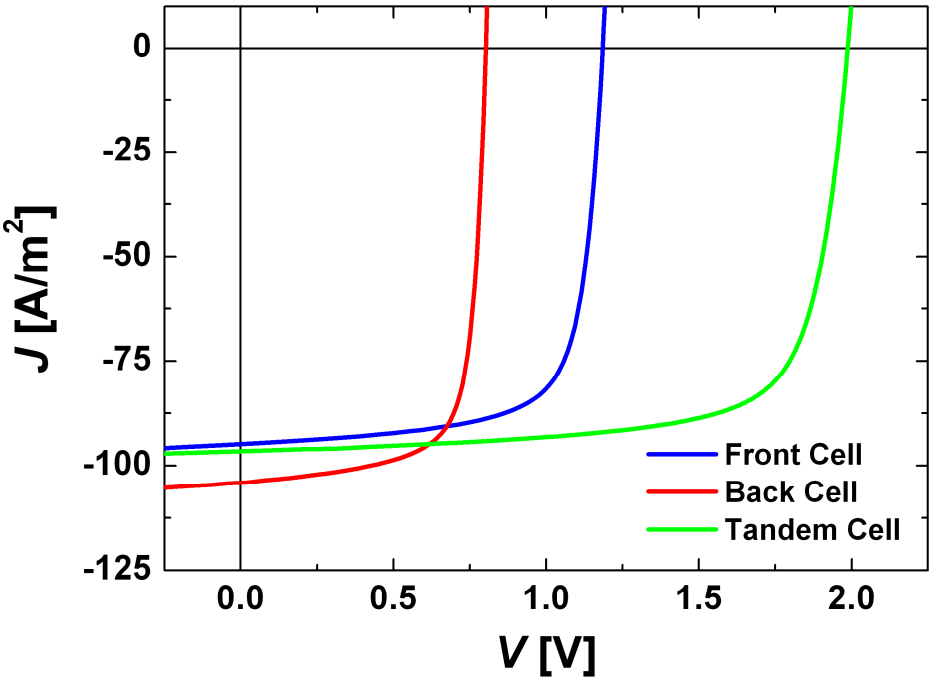

Figure 6.5: Current density J as a function of potential difference V between the contact electrodes of both subcells and the tandem cell. The potential difference of the tandem cell is a simple addition of the potential differences of the subcells when their J is equal.

As the subcell with the narrowest band gap has a broader absorption spectrum it is more profitable to situate the narrower band gap subcell in the back of the tandem cell. The reverse situation, represented by the local maximum of η = 13.1 % in Figure 6.4 at B_{gap}^{front} = 1.4 eV, B_{gap}^{back} = 1.9 eV, FLT = 40 nm, and BLT = 200 nm, shows that the overlap of the absorption spectra leads to a reduction of the photon influx into the back subcell, leading to a decrease of the optimum FLT for the narrower band gap subcell and an increase of BLT for the wider band gap subcell. It should be noted that

the η_{max} calculated here assumed [60]PCBM as the electron acceptor. The recent efficiency records reported for polymer:fullerene solar cells[12] all used [70]PCBM as an acceptor, in combination with a low band gap polymer. Since [70]PCBM absorbs in the visible, the absorption spectrum of the solar cell is broadened, leading to more absorption and higher efficiencies. This spectral broadening, however, makes it more difficult to exploit these cells in tandem structures since the second subcell will need to be shifted more to the infrared in order to be complementary with the broadened spectrum of the present low band gap record cells. So far, efficient solar cells based on these (near) infrared materials are not yet available, but when present they will open a route toward tandems that are able to exceed 14 % efficiency.

6.4 Conclusions

In conclusion, the ultimate efficiency of organic tandem solar cells has been calculated using a combined optical and electrical device model. With this model the efficiencies of single cells have been evaluated as a reference, leading to a maximum efficiency of 11.7 %. For tandem structures using a ZnO/PEDOT:PSS middle electrode an ultimate efficiency of 14.1 % has been calculated. As a result tandem structures are expected to give a performance improvement of about 20 % as compared to single cells.

References

[1] M. C. Scharber, D. Mühlbacher, M. Koppe, P. Denk, C. Waldauf, A. J. Heeger, and C. J. Brabec, Adv. Mater. **18**, 789 (2006).

[2] L. J. A. Koster, V. D. Mihailetchi, and P. W. M. Blom, Appl. Phys. Lett. **88**, 093511 (2006).

[3] L. J. A. Koster, E. C. P. Smits, V. D. Mihailetchi, and P. W. M. Blom, Phys. Rev. B **72**, 085205 (2005).

[4] J. D. Kotlarski, P. W. M. Blom, L. J. A. Koster, M. Lenes, and L. H. Slooff, J. Appl. Phys. **103**, 084502 (2008).

[5] G. Dennler, M. C. Scharber, T. Ameri, P. Denk, K. Forbeich, C. Waldauf, and C. J. Brabec, Adv. Mater. **20**, 579 (2008).

[6] A. Hadipour, B. de Boer, and P. W. M. Blom, Adv. Funct. Mater. **18**, 169 (2008).

[7] J. Gilot, M. M. Wienk, and R. A. J. Janssen, Adv. Mater. **22**, E67 (2010).

[8] D. R. Lide, *Handbook of Chemistry and Physics*, CRC, Boca Raton, 1994).

[9] H. Hoppe, N. S. Sariciftci, and D. Meissner, Mol. Cryst. Liq. Cryst. Sci. Technol., Sect. A **385**, 113 (2002).

[10] M. M. Mandoc, L. J. A. Koster, and P. W. M. Blom, Appl. Phys. Lett. **90**, 133504 (2007).

[11] V. D. Mihailetchi, H. Xie, B. de Boer, L. M. Popescu, J. C. Hummelen, P. W. M. Blom, and L. J. A. Koster, Appl. Phys. Lett. **89**, 012107(2006).

[12] Y. Liang, Z. Xu, J. xia, S. T. Tsai, Y. Wu, G. Li, C. Ray, and L. Yu, Adv. Mater. **22**, E315 (2010).

[13] J. Gilot, M. M. Wienk, and R. A. J. Janssen, Appl. Phys. Lett. **90**, 143512 (2007).

[14] D. Moet, P. de Bruyn, J. D. Kotlarski, and P. W. M. Blom, Org. Electron. **11**, 1821 (2010).

[15] T. Ameri, G. Dennler, C. Lungenschmied, and C. J. Brabec, Energy Environ. Sci. **2**, 347 (2009).

List of publications

1. **J. D. Kotlarski**, P. W. M. Blom, L. J. A. Koster, M. Lenes, and L. H. Slooff, *Combined optical and electrical modeling of polymer:fullerene bulk heterojunction solar cells*, J. Appl. Phys. **103**, 084502 (2008).

2. D. J. D. Moet, M. Lenes, **J. D. Kotlarski**, S. C. Veenstra, J. Sweelsen, M. M. Koetse, B. de Boer, and P. W. M. Blom, *Impact of molecular weight on charge carrier dissociation in solar cells from a polyfluorene derivative*, Org. Electron. **10**, 1275 (2009).

3. D. J. D. Moet, **J. D. Kotlarski**, and P. W. M. Blom, *Enhanced efficiency in double junction polymer:fullerene solar cells*, Org. Electron. **11**, 1821 (2010).

4. **J. D. Kotlarski** and P. W. M. Blom, *Ultimate performance of polymer:fullerene bulk heterojunction solar cells*, Appl. Phys. Lett. **98**, 053301 (2011).

5. **J. D. Kotlarski**, D. J. D. Moet, and P. W. M. Blom, *Role of balanced charge carrier transport in low band gap polymer:fullerene bulk heterojunction solar cells*, J. Polym. Sci. Part B: Polym. Phys. **49**, 708 (2011).

6. **J. D. Kotlarski** and P. W. M. Blom, *Impact of unbalanced charge transport on the efficiency of normal and inverted solar cells*, Applied Physics Letters **100**, 013306 (2012).

Summary

The worldwide demand for usable energy increases year after year and feasible alternatives for fossil fuels need to be employed in order meet that demand. Organic photovoltaics are expected to contribute in meeting that demand and are already in commercial production. In the past two decades, interest in organic solar cells was boosted by the discovery of photo-induced very fast electron transfer from conjugated polymers to fullerenes, leading to the development of bi-layer solar cells using these materials as active layers. In the following years new photo-receptive polymer semiconductors and electron-accepting materials were discovered and utilized. Furthermore, new methods were developed how to increase the effective interfacial contact area between the photo-receptor and the electron-accepting materials in the solar cells. In particular blending of the electron-accepting and electron-donating material in a nanoscopic bulk heterojunction significantly increased the performance of solar cells based on polymer donors and fullerene acceptors. The efficiency of organic polymer:fullerene bulk heterojunction solar cell performance has been steadily increasing in the last decade, going from 2.5 % efficiency in 2001 to 3.5 % in 2003, up to 5.5 % in 2007, and recently an efficiency of 8.3 % has been reported.

In the further pursuit of better performing organic bulk heterojunction solar cells, predicting the limit of their performance is important. In the past years, theoretical studies have been undertaken to understand what the fundamental performance limits are for organic bulk heterojunction solar cells. These studies predict a practical power conversion efficiency limit of about 10 to 11 % for single cells. Efficiency calculations done by Koster *et al.* employed a detailed electrical model including field- and temperature dependent dissociation of bound electron – hole pairs as well as space-charge formation in the case of unbalanced charge

transport. The model was based on the assumption that the optical profile can be taken as constant and that the photocurrent is directly dependent on the total amount of absorbed photon flux.

In chapter 2 we introduce the transfer matrix formalism describing the coherent passage of light through thin film layer stacks using elementary formulaic descriptions in 2 by 2 matrices. These are multipliable with each other and are used to calculate electric fields of light travelling in opposite directions in one position inside the layer stack denoted as a 1 by 2 electric field vector from another electric field vector in another position. First the basic equations governing propagation and refraction of plane light waves perpendicular to and in sunlight coherent thin layers are given. Then the transfer matrix model is introduced, including matrix multiplication, descriptions of transmission and reflection and propagation and refraction equations in matrix form in order to model optical interference. Optical interference effects are important for the total absorption as well as the profile of the exciton generation rate in polymer:fullerene bulk heterojunction solar cells.

For solar cells with an active layer of poly[2-methoxy-5-(3′,7′-dimethyloctyloxy)-1,4-phenylenevinylene] (MDMO-PPV) as electron donor and [6,6]-phenyl C_{61} butyric acid methyl ester (PCBM) as electron acceptor the total exciton generation rate can be directly extracted from the saturated photocurrent. In chapter 3 it is demonstrated that for solar cells with an active layer thickness smaller than 250 nm a constant exciton generation profile, based on this extracted total rate, gives identical electrical characteristics as compared to exciton generation profiles from an optical model. For thicker cells interference effects have to be taken into account, since a uniform generation profile leads to an overestimation of recombination losses and space-charge formation.

The performance improvement of organic solar cells in recent years mainly originated from the development of low band gap polymers, of which the absorbance has an enhanced overlap with the solar spectrum. However, lowering of the optical band gap of conjugated polymers in bulk heterojunction solar cells not only leads to an increased absorption but also to an increase of the optimal active layer thickness due to interference effects at longer wavelengths. The increased carrier densities due to the enhanced absorption and thicker active layers make low band gap solar cells

more sensitive to formation of space-charges and recombination. By systematically red-shifting the optical parameters of MDMO-PPV and PCBM we show in chapter 4 the effect of a reduced band gap on the solar cell efficiencies. Especially the fill factor of low band gap cells is very sensitive to the balance of the charge transport. For a low band gap cell with an active layer thickness of 250 nm the fill factor of 50 % for balanced transport is reduced to less than 40 % by an imbalance of only one order of magnitude.

In a typical organic solar cell most charge carriers are generated close to the anode, such that electrons have to travel a longer distance as compared to the holes. In an inverted solar cell holes have to travel a longer distance. In chapter 5 the effect of unbalanced transport on the efficiency of normal and inverted single- and tandem solar cells is described. When the electrons are ten times more mobile than the holes the efficiency for a single cell with a thickness of 250 nm drops from 7.5 to 4.5 % when changing from a normal to an inverted structure. For opposite mobility ratio the inverted structure clearly outperforms the normal structure. In tandem structures a similar effect can be observed when switching between normal and inverted structures when looking at any kind of unbalanced charge transport.

Based on optical considerations for organic tandem solar cells the maximum efficiency was estimated to be around 14 %. In chapter 6 model calculations are presented to explore the maximum efficiency of polymer:fullerene tandem solar cells, using a combined optical- and electrical device model, where the absorption profiles are used as starting point for the numerical current-voltage calculations. With this model a maximum power efficiency of 11.7 % for single cells has been achieved as a reference. For tandem structures with a ZnO/PEDOT:PSS middle electrode an ultimate efficiency of 14.1 % has been calculated. In the optimum configuration the sub-cell with the narrowest band gap is placed closest to the incoming light. Consequently, tandem structures are expected to enhance the performance of optimized single cells by about 20 %.

Samenvatting

De wereldwijde vraag naar bruikbare energie wordt elk jaar groter en uitvoerbare alternatieven voor fossiele brandstoffen zullen ingezet moeten worden om aan die vraag te voldoen. Organische fotovoltaïsche cellen worden verwacht om aan een deel van die vraag zullen voldoen en zijn al in commerciële productie. In de laatste twee decennia, interesse in organische zonnecellen werd versterkt door de ontdekking van foto-geïnduceerde heel snelle elektronenoverdracht van geconjugeerde polymeren naar fullerenen, wat leidde tot de ontwikkeling van bi-laag zonnecellen die deze materialen als actieve lagen gebruiken. In de navolgende jaren werden nieuwe fotoreceptieve polymere halfgeleiders en elektronen-accepterende materialen ontdekt en toegepast. Verder werden er nieuwe methoden ontwikkeld om het effectieve contactgrensoppervlak tussen de fotoreceptor en de elektronen-accepterende materialen in de zonnecellen te vergroten. In het bijzonder leidt de vermenging van elektronen-accepterende en elektronen-donerende materialen in een nanoscopische bulk heterojunctie tot een aanzienlijke verhoging van het prestatievermogen van zonnecellen die op polymere donoren en fullerene acceptoren gebaseerd zijn. De efficiëntie van organische polymeer:fullereen bulk heterojunctie zonnecellen is het laatste decennium gestaag gestegen, gaande van 2.5 % efficiëntie in 2001 naar 3.5 % in 2003, op naar 5.5 % in 2007 en recentelijk is er een efficiëntie van 8.3 % gemeld.

In het streven naar beter presterende organische bulk heterojunctie zonnecellen, is het belangrijk om de limiet van hun prestatievermogen te kunnen voorspellen. In de afgelopen jaren zijn theoretische studies ondernomen om de fundamentele limieten voor het prestatievermogen van bulk heterojunctie zonnecellen te begrijpen. Deze studies voorspellen een praktische limiet van vermogensomzetting

van rond de 10 a 11 % voor enkele cellen. Efficiëntieberekeningen uitgevoerd door Koster *et al.* pasten een gedetailleerd elektrisch model toe dat gebruik maakt van veld- en temperatuurafhankelijke dissociatie van gebonden elektron – gat paren als ook ruimte-ladingsformatie in het geval van ongebalanceerd ladingstransport. Het model is gebaseerd op de aanname dat het optische profiel als een constante gezien kan worden en dat de fotostroom direct afhankelijk is van de totale hoeveelheid geabsorbeerde fotonenflux.

In hoofdstuk 2 introduceren wij het overdrachtsmatrix model, dat de coherente doorgang van licht door stapels van dunne filmlagen beschrijft middels elementaire formule beschrijvingen in 2 bij 2 matrices. Deze zijn met elkaar vermenigvuldigbaar en worden gebruikt om de elektrische velden van het licht in een bepaalde positie, hetwelk in beide tegengestelde richtingen reist, genoteerd als een 1 bij 2 elektrische veldvector te berekenen vanuit een andere elektrische veldvector in een andere positie. Eerst worden de basale vergelijkingen gegeven, die de voortplanting en refractie van vlakke lichtgolven loodrecht op en in zonlicht coherente dunne lagen beschrijven. Dan wordt het overdrachtsmatrix model geïntroduceerd, inclusief matrixvermenigvuldiging, beschrijvingen van transmissie en reflectie en voortplantings- en refractievergelijkingen in matrixvorm om optische interferentie te modelleren. Optische interferentie effecten zijn belangrijk voor zowel de totale absorptie als het profiel van de snelheid van exciton-generatie in polymeer:fullereen bulk heterojunctie zonnecellen.

Voor zonnecellen met een actieve laag van poly[2-methoxy-5-(3′,7′-dimethyloctyloxy)-1,4-phenylenevinyleen] (MDMO-PPV) als elektronendonor en [6,6]-phenyl C_{61} butyric acid methyl ester (PCBM) als elektronenacceptor kan de totale snelheid van exciton-generatie direct uit de verzadigde fotostroom geëxtraheerd worden. In hoofdstuk 3 wordt gedemonstreerd dat zonnecellen met een actieve laag dunner dan 250 nm met een constant exciton-profiel, gebaseerd op deze geëxtraheerde totale snelheid, identieke elektrische karakteristieken geven wanneer vergeleken met exciton-generatieprofielen voortkomend uit een optisch model. Voor dikkere cellen moeten interferentie-effecten in ogenschouw genomen worden, daar een uniform generatieprofiel tot een overschatting van recombinatieverliezen en ruimtelading formative leidt.

De verbetering van het prestatievermogen van organische zonnecellen in recente jaren komt voornamelijk voort uit de ontwikkeling van lage bandkloof polymeren, waarvan de absorptie een betere overlap met het zonnespectrum heeft. Echter, het verlagen van de optische bandkloof van geconjugeerde polymeren in bulk heterojunctie zonnecellen leidt niet alleen tot een verhoogde absorptieve, maar ook tot een toename van de optimale dikte van de actieve laag vanwegen interferentie-effecten voor langere golflengten. De verhoogde ladingsdragerdichtheden door de verbeterde absorptie en dikkere actieve lagen zorgen ervoor dat lage bandkloof zonnecellen gevoeliger zijn voor de vorming van ruimteladingen en recombinatie. Door een systematische roodverschuiving van de optische parameters van MDMO-PPV en PCBM laten we in hoofdstuk 4 het effect van een gereduceerde bandkloof op de zonneceleffici$\ddot{e}$nties zien. Bij uitstek de vulfactor van lage bandkloof cellen is uiterst gevoelig voor de balancering van het ladingstransport. Voor een lage bandkloof cel met een actieve laagdikte van 250 nm wordt de vulfactor van 50 % voor gebalanceerd transport verlaagd tot minder dan 40 % voor een onevenwicht van maar een ordegrootte.

In een typische organische zonnecel worden de meeste ladingsdragers in dichtbij de anode gegenereerd, zodat de elektronen een langere afstand afleggen wanneer vergeleken met de gaten. In een geïnverteerde zonnecel leggen gaten een langere afstand af. In hoofdstuk 5 wordt het effect van ongebalanceerd ladingstransport op de efficiëntie van normale en geïnverteerde enkele en tandem zonnecellen beschreven. Wanneer elektronen een tien keer hogere mobiliteit dan gaten hebben, daalt de efficiëntie voor een enkele cel met een dikte van 250 nm van 7.5 naar 4.5 % bij verandering van een normale naar een geïnverteerde structuur. Voor een omgekeerde mobilitieitsverhouding overtreft het prestatievermogen van de geïnverteerde structuur dat van de normale structuur. In tandem structuren met ongebalanceerd ladingstransport kan een vergelijkbaar effect geobserveerd worden wanneer er tussen normale en geïnverteerde structuren omgeschakeld wordt.

Gebaseerd op optische overwegingen voor organische tandem zonnecellen wordt hun maximum efficiëntie geschat rond de 14%. In hoofdstuk 6 worden berekeningen gepresenteerd om de maximum efficiëntie van polymeer:fullereen tandem zonnecellen te verkennen middels het gebruik van een gecombineerd optisch en elektrisch model, waarbij de absorptieprofielen gebruikt worden als een startpunt voor de numerieke stroom-spanning berekeningen. Met behulp van dit model werd

een enkele cel maximum vermogensefficiëntie van 11.7 % behaald als referentie. Voor tandem structuren met een ZnO/PEDOT:PSS middenelectrode werd een ultieme efficiëntie van 14.1 % berekend. In de optimale configuratie is de subcel met de nauwste bandkloof het dichtst bij het inkomende licht geplaatst. Derhalve is de verwachting dat tandem structuren het prestatievermogen van geoptimizeerde enkele cellen met ongeveer 20 % verhoogd.

Acknowlegdments

Nearly seven years ago I started on this journey of being a PhD student, not knowing what lay await for me. Photo-switchable polymers were the original subject of my thesis, but after about half a year Paul Blom suggested a different subject to me because things weren't progressing well with the original project due to personal problems. Thus I switched to optical modeling of polymer solar cells, designing a self-written program in Delphi. It has been a difficult road since then, but I am glad and thankful that I could persevere in midst of adversity, with the help of God, family, colleagues and friends. Without your help people, I would have been ship-wrecked years ago.

I thank you, Paul, for bearing with me all these years, you really helped me through with your positive attitude and encouragement. It was quite difficult having you as my promoter mostly gone in the past few years, but due to your help and advice this thesis and the research it rests upon have been concluded and a new chapter in life awaits me.

Bert de Boer is still in my fond memories, whose death was a shock for the MEPOS group. I still fondly think back to the few times I did ask him for advice and also to those times where he woke me up during talks, when I fell asleep due to sleep deprivation. I do miss him, as do many still in the group.

Jan-Anton, you have been so helpful when you were here, when you were away and when you were here again. I totally appreciate your assistance through and with SIMsalabim and the talks we had.

Lenneke, thank you for your contribution to my articles and the few talks we had about organic solar cells. Jan, you helped me a lot and especially with the many "counseling talks" we had, you were a mentor of sort for me. Afshin, I appreciate the

wisdom you shared with me in those early years, you were a kind of big brother to me. Renate, thank you for encouraging me during these last years, you were like a big sister to me, who did administrative work as well. Frans, we kept having really nice conversations and I thank you for all your help, especially with the PC problems I experienced.

Franscesco, I think we had too much fun in all these years, インポッシブル!

Irina, thank you very much for helping me out that much with my thesis. Yuan, thanks for being such a fun guy.

Further thanks go out to all other (former) members of the MEPOS groups, I appreciate talking to you and having you as colleagues/group members: Minte, Teunis, Valy, Cristina, Denis, Andre, Ronald, Magda, Denis, Hylke, René, André, Martijn L., Auke, Kamal, Maria, Eek, Hennie, Date, Dorota, Fabrizio, Edsger, Jia, Ilias, Davood, Jolt, Simone, Dago, Kees, Maria, Jurjen, Arjen, Ryan, Martijn K., Johan, Davood, Ilias, Claudia, Mark-Jan, Anne-Marije, Fatemeh, Milo, Paul, Gert-Jan, Herman, Alex, Widi, Kriszti, Marianna, Stephen, Ameneh, Laaya, Tondo, Mark, Gerjan, Vladimir and Niels.

Maxim, thank you for your recommendations and help. Sigrid, thank you for your help and friendship, you were there when I needed it most. Dirk-Jan and Marga, you are both dear friends of mine, I just wish I was more of a friend to you. Niko, I appreciated the times you visited. Martijn R., I enjoy our friendship and thank you for your patience. Egbert, you were patient as well and I appreciate that you were there for me. Joey, a good friend and more of mine, thank you for putting up with me as well. Els, thank you for your professional advice and help. Uschi, thank you for your advice and friendship, my aunt and sister in Christ. Harry en Gea, jullie waren in al die jaren trouwe vrienden en een fijne broeder en zuster, dank jullie ook daarvoor. Willem and Harriët, dank jullie voor alle hulp in de laatste jaren. Veel dank aan al mijn broeders en zusters van het Nationaal Kruisleger. Ook veel dank aan al mijn andere broeders en zusters in Christus Jezus die mij kennen. Many thanks to all my brothers and sisters in Jesus Christ who know me.

My dear paranymphs, I did not know your names yet when this thesis was put forward to the printer, yet I still want to thank you for accepting the daunting task of helping me on my promotion. You may still have many tasks left and hopefully when everything is over we will be celebrating and laughing.

For the last but not least I want to thank You, heavenly Father, for leading me with Your Holy Spirit. Yes, I was rebellious and foolish, doing whatever I wanted. But thanks to Your provision through Your Son Jesus Christ am I restored and willing again. If it weren't for You, Saviour and Lord Jesus, I'd be hopeless and wretched, but due to You keeping my faith in You, I have eternal life from You and a mission to fulfill. Thank You so much for doing all and more for me and my brothers and sisters in You.